Journal of Energy Storage 153 (2026) 120542

Contents lists available at ScienceDirect

Journal of Energy Storage

journal homepage: www.elsevier.com/locate/est

Research Papers

# Collaborative optimization operation method of electrical-thermal-hydrogen multi-energy storage system based on variable mode decomposition

Di Wu [a,b], Shiyang Yu [a], Ao Liu [a], Zhijian Liu [a,b,*], Zhuoying Liang [a], Shicong Zhang [c], Xinyan Yang [c], Guiqiang Li [d], Wentao Wu [e]

[a] Department of Power Engineering, School of Energy, Power and Mechanical Engineering, North China Electric Power University, Baoding, 071003, Hebei, China
[b] Hebei Key Laboratory of Energy Storage Technology and Integrated Energy Utilization, North China Electric Power University, Baoding, 071003, Hebei, China
[c] Institute of Building Environment and Energy, China Academy of Building Research, Beijing, 100013, China
[d] Department of Thermal Science and Energy Engineering, University of Science and Technology of China, Hefei, 230026, Anhui, China
[e] School of Built Environment, Massey University, Auckland, New Zealand

ARTICLE INFO

*Keywords:*
Variational mode decomposition
Multi-energy storage
Cost evaluation
Optimizing operation
Experimental validation

ABSTRACT

The integration and utilization of renewable energy into the grid is key to building a clean and low-carbon energy system, but its intermittency and volatility cause significant wind and solar curtailment. To address this, this paper proposes a multi-energy storage system integrating electrical, thermal, and hydrogen storage. The system firstly uses Variational Mode Decomposition (VMD) to decompose and reconstruct the power difference between the source and the load. The power allocation based on the dynamic response characteristics of supercapacitors, hydrogen storage, and thermal storage tanks. Three progressive operating strategies are designed: baseline power allocation based on VMD (Strategy 1), adaptive VMD adjustment considering the state of charge (SOC) of energy storage (Strategy 2), and coordinated optimization introducing grid regulation (Strategy 3). An experimental platform focused on lithium batteries and supercapacitors was built to verify the feasibility of the power allocation and real-time adjustment strategies. Furthermore, the experimentally validated control strategies were applied to a simulation case of a Beijing community to conduct system modeling based on a physical model. Results show that Strategy 3 achieves zero SOC violation in energy storage, significantly outperforming Strategy 1 (which had a 47.5% violation rate) and Strategy 2 (37%), with operational costs reduced by 13.3% and 17.7% compared to Strategies 1 and 2, respectively, and a system excess capacity ratio of 0%. The conclusions indicate that the proposed VMD-based multi-energy storage coordinated optimization method, especially Strategy 3 combined with grid regulation, can effectively enhance system stability and economy, providing an effective solution for multi-energy system management in scenarios with a high proportion of renewable energy.

## 1. Introduction

Renewable energy penetration has increased significantly, yet its consumption remains relatively low. In China, wind power abandonment rates reached 12% in Gansu and over 20% in Inner Mongolia in 2022 [1]. Similarly, Gansu and Ningxia reported photovoltaic curtailment rates of 10%–15% in 2023 [2]. Countries such as India [3], the US [4], Brazil [5], Australia [6], and Saudi Arabia [7] also face abandonment rates between 10% and 20% [8]. In this context, the integration of multi-energy storage systems has become crucial for the development of clean, low-carbon energy. Among various energy sources, hydrogen energy, known for its high calorific value, pollution-free characteristics, and superior performance, plays a vital role in the multi-energy storage systems [9]. For the energy distribution of multiple storage devices, Variational Mode Decomposition (VMD) systems offer many advantages [10]. VMD can serve as an important tool for power frequency allocation in multi-energy storage systems.

Currently, extensive research has been conducted on multi-energy storage system, but three core research gaps remain that urgently need to be addressed. First, in terms of system composition, most studies focus on the electro-thermal binary energy storage model [11–14,22–24]. Although some literatures involve hydrogen energy integration [25–32], they primarily focus on the basic aspects of wind

* Corresponding author at: North China Electric Power University Department of Power Engineering, Baoding, 071003, Hebei, China.
*E-mail address:* zhijianliu@ncepu.edu.cn (Z. Liu).

https://doi.org/10.1016/j.est.2026.120542
Received 7 September 2025; Received in revised form 10 January 2026; Accepted 12 January 2026
Available online 3 February 2026

**Nomenclature**

*Symbols and acronyms*

| | |
|---|---|
| A | Area($m^2$) |
| C | Capacitance, Cost(USD) |
| ECR | Excess Capacity Ratio |
| EL | Electrolyzer |
| F | Faraday constant(C/mol) |
| FC | Fuel Cell |
| HESS | Hydrogen Energy Storage System |
| HP | Heat Pump |
| HST | Hydrogen Storage Tank |
| I | Current, Investment cost(USD) |
| IMF | Intrinsic Mode Function |
| K | Number of VMD modes |
| M | Molar mass(g/mol) |
| N | Number, Service life(year) |
| P | Power(kW) |
| PV | Photovoltaic |
| RMSE | Root Mean Square Error |
| MAE | Mean Absolute Error |
| SC | Supercapacitor |
| S | Unit cost(USD/kW, USD/kg, etc.) |
| SOC | State of Charge |
| T | Temperature(K, °C) |
| U | Voltage(V) |
| VMD | Variational Mode Decomposition |
| V | Volume($m^3$) |
| WST | Water Storage Tank |
| n | Molar production/consumption rate(mol/s) |
| v | Hydrogen production/consumption rate(mol/s) |
| f | Filter constant, Input signal |
| k | Empirical factor |

*Greek symbols*

| | |
|---|---|
| α | VMD penalty parameter |
| β | Temperature coefficient |
| δ | Heat loss coefficient, Dirac delta function |
| η | Efficiency |
| ω | Center frequency (VMD) |
| u | Mode function (VMD) |
| Φ | Phase (VMD) |

*Subscripts*

| | |
|---|---|
| 0 | Initial or standard condition |
| amb | Ambient |
| bat | Battery |
| chr | Charging |
| dis | Discharging |
| ex | Export/outlet |
| H | High-frequency component |
| $H_2$ | Hydrogen |
| im | Import/inlet |
| L | Low-frequency component |
| M | Medium-frequency component |
| max | Maximum |
| min | Minimum |
| noct | Nominal operating cell temperature |
| ref | Reference/standard condition |
| h/c | Heating/Cooling |

and solar energy storage capacity configuration, electricity-hydrogen hybrid energy storage scheduling, and often neglect to model the waste heat generated by fuel cells (FC) and electrolyzers (EL). Secondly, regarding system regulation, existing research predominantly focuses on peak shaving [33–36], and the research on frequency modulation of complex multi-energy storage system, especially the precise power distribution, particularly scarce, which makes it difficult to meet the stringent power quality requirements of the grid. Thirdly, in terms of research methodology, most of the studies remain largely at the theoretical simulation stage [11–21,25–32]. Even though a few studies have constructed experimental platforms [40,41], most of these are only basic setups and are inadequate for thorough verification of the proposed control strategies and models. This limitation significantly constrains the engineering applicability and transformation value of the research outcomes. In the application of power distribution algorithms, although VMD and its improved versions have been studied for optimizing hybrid energy storage systems [37–39], the existing implementations have not been specifically designed to account for the cooperative characteristics of multi-energy systems involving electricity, heat, and hydrogen. This differs fundamentally from the customized application of VMD for multi-energy complementary scenarios proposed in this study. In recent years, some scholars have made preliminary explorations on the utilization of residual heat of hydrogen energy storage [42] and the adaptation and optimization of VMD in multi-energy scenarios [43], but a complete multi-energy collaborative solution has not yet been formed, and there is still room for expansion in related research.

Summary: To address the gaps in existing research in four dimensions—energy storage system composition, control direction, practical validation, and algorithm adaptation—this paper proposes a multi-energy storage system encompassing electricity, hydrogen, and heat. It establishes a complete thermodynamic model of the system, applies a customized VMD method for optimized power distribution, and sets up a dedicated experimental platform for empirical research. Through a real case in a community in Beijing, the advantages of the system in operational performance, reliability, and economic efficiency are comprehensively verified, providing theoretical support and practical reference for the engineering application of multi-energy storage systems.

The innovation and main contribution of this study closely revolve around the above research gaps and are manifested in the following targeted solutions. In this paper, firstly, an electric-thermal-hydrogen multi-energy energy storage system is constructed and the corresponding thermodynamic model is established. Different from the limitation that the existing hydrogen energy-related research only focuses on electric energy conversion, the waste heat generated during the operation of FCs and electrolyzers is recovered to the thermodynamic circuit, which realizes the electric-thermal synergistic utilization of hydrogen energy and significantly improves the comprehensive energy efficiency of the system. At the same time, the variational modal decomposition (VMD) method is used to decompose and reconstruct the source-load power difference, and then determine the output power of various energy storage devices. Compared with previous studies based on AHA-VMD algorithm and adaptive VMD, the VMD application in this study fully combines the dynamic characteristics of multi-energy complementation of electricity, heat and hydrogen, and realizes the customization and accuracy of power distribution, filling the gap in the tailored application of VMD in multi-energy collaborative scenarios. Secondly, a dedicated experimental platform for multi-energy storage systems was constructed. This platform enables systematic analysis of the dynamic response characteristics of supercapacitors and batteries under different working conditions, which provides solid experimental verification support for the research results and thereby addressing the common limitation of lacking empirical validation in most studies. Finally, taking a community in Beijing as an application case, the proposed electric-thermal-hydrogen multi-energy energy storage system is applied to

meet the energy demands, and three operation strategies are designed to optimize the system performance. By comparing and analyzing the characteristics of state-of-charge (SOC) curves of hydrogen storage, heat storage and electricity storage equipment, as well as the over-limit operation time ratio and system operation cost of various energy storage equipment, it provides a practical engineering scheme for frequency modulation and power distribution of complex multi-energy energy storage systems, and makes up for the shortcomings of lack of practical research in this field.

To better understand the research in this paper, Fig. 1 is a flowchart of the entire work.

To more clearly position this study, Table 1 compares this research with representative literature across key dimensions.

## 2. Electrical-thermal-hydrogen multi-energy storage system

### 2.1. System structure

The system structure is depicted in Fig. 2. It illustrates the structure of the electrical-thermal-hydrogen multiple energy storage system. The system consists of photovoltaic panel(PV), supercapacitor(SC), hydrogen storage system(HESS) (electrolyzer(EL), hydrogen storage tank(HST), fuel cell(FC)), compression heat pumps(HP), storage tanks (WST) and municipal power grids.

The electrical load of the users is supplied by the PV, FC and SC. The cooling and heating loads are provided by the HP. If the HP output is insufficient to meet the cooling or heating load, the WST can provide supplemental energy. The WST functions as a heat storage tank in winter and a cold storage tank in summer. The excess electrical energy generated by the PV can be stored in the HST and SC. Similarly, excess thermal energy generated by the HP can be stored in the WST. The waste heat from the FC and EL is recovered and used directly to meet user heating demands. Any surplus heat is stored in the WST during winter. The detailed principles of the VMD frequency control strategy are presented in Section 3.1.

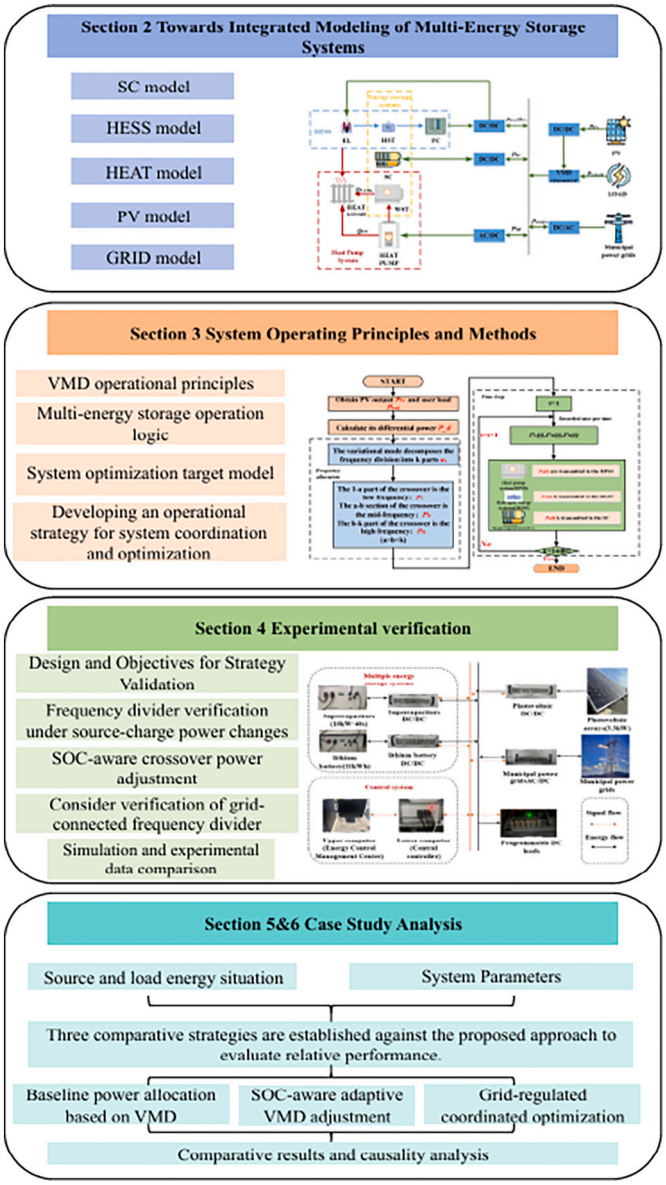


**Fig. 1.** Overall main workflow diagram.

**Table 1**
Comparative analysis of this study with representative literature.

| Features | Typical electricity-heat studies [11,14] | Typical electricity-hydrogen studies [25,27] | Typical VMD Applications [39,40] | This study |
|---|---|---|---|---|
| Types of energy storage owned | Electricity, Heat | Electricity, Hydrogen | Electricity (Battery, SC) | Electricity, heat, hydrogen |
| Core method | Economic dispatch | Capacity configuration | VMD for power allocation | VMD + Three-tier adaptive control |
| Validation | Simulation | Simulation | Simulation | Experiment + Simulation |
| Primary focus | Cost, peak shaving | Reliability, capacity | Power smoothing | Frequency allocation, SOC management, cost-saving synergy |

### 2.2. Mathematical model of the system

#### 2.2.1. Photovoltaic panel(PV)

The performance of photovoltaic panels is mainly affected by the hourly ambient temperature and solar irradiance. It is determined by the temperature of the solar cells. The amount of electricity generated by photovoltaic panels ($P_{PV}(t)$,kW) is determined by the following equations [44]:

$$T_{PV}(t) = T_{amb}(t) + \frac{(T_{noct} + T_{ref})G(t)}{G_{ref}} \quad (1)$$

$$\eta_{PV}(t) = \eta_{PV,0}\left(1—\beta_{PV}\left(T_{PV}(t)—T_{ref}\right)\right) \quad (2)$$

$$P_{PV}(t) = A_{PV}\eta_{PV}(t)G(t)\eta_{inverter} \quad (3)$$

where $T_{amb}(t)$ and $T_{PV}(t)$ are the ambient temperature and the temperature of the solar cell at time $t$,°C. $G(t)$ is the solar irradiance at time $t$, W/m$^2$. $T_{noct}$ and $T_{ref}$ are the battery temperature and standard temperature under standard operating conditions, °C. $G_{ref}$ is the solar irradiance under standard conditions, W/m$^2$. $\eta_{PV}(t)$ is the efficiency of power generation at time $t$.$\eta_{PV,0}$ is the power generation efficiency under the standard condition. $\beta_{PV}$ is the temperature coefficient. $P_{PV}(t)$ is the electrical power output by photovoltaic cells at time $t$, kW. $A_{PV}$ is the area of a single solar PV panel, m$^2$. $\eta_{inverter}$ is the efficiency of the inverter.

#### 2.2.2. Supercapacitor (SC)

The operation model of the SC and the corresponding operational constraints are shown in Eqs. (4) and (5) [45]:

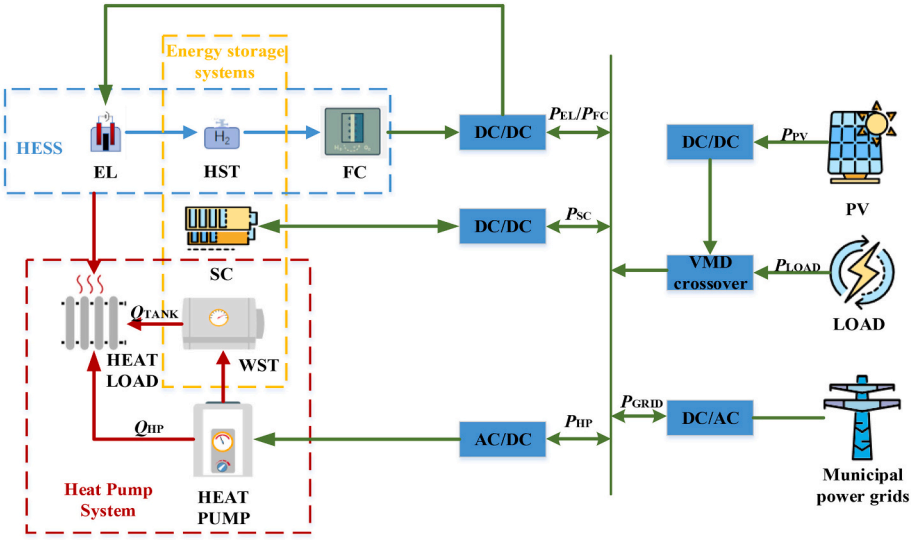


**Fig. 2.** The structure of the multi-element energy storage system.

$$SOC_{sc}(t) = SOC_{sc0} - \int_0^t \frac{U_{sc} i_{sc}}{0.5 C_{sc} V_{sc,max}^2} dt \tag{4}$$

$$\begin{gathered} U_{sc,chr}^t = 1 \Big/ U_{sc,dis}^t = 1 \\ U_{sc,chr}^t P_{sc,chr}^{min} \le P_{sc,chr}^t \le U_{sc,chr}^t P_{sc,chr}^{max} \\ U_{sc,dis}^t P_{sc,dis}^{min} \le P_{sc,dis}^t \le U_{sc,dis}^t P_{sc,dis}^{max} \\ U_{sc,chr}^t + U_{sc,dis}^t \le 1 \\ SOC_{sc}^t = SOC_{sc}^{t-1} + \eta_{sc,chr} P_{sc,chr}^t \Delta t - \frac{P_{sc,dis}^t}{\eta_{sc,dis}^t} \Delta t \\ SOC_{sc}^{min} \le SOC_{sc}^t \le SOC_{sc}^{max} \end{gathered} \tag{5}$$

where $SOC_{sc}(t)$ is the capacitance state of the SC at time $t$. $SOC_{sc0}$ is the initial state of the SC. $V_{sc}$, $i_{sc}$ and $C_{sc}$ are the voltage, current and capacitance of the SC, V,A,F. $U_{sc,max}$ is the maximum voltage of the SC, V. $U_{sc}$ is the real-time voltage of the SC, V. Constraint (5a) ensures that the SC operates exclusively in either charging or discharging mode. *Ut sc,chr* and *Ut sc,dis* are the charging and discharging voltage for the SC at time *t*, V. *Pmin sc,chr* and *Pmax sc,chr* are the minimum and maximum charging power of the SC, W. *Pt sc,chr* and *Pt sc,dis* are the charge and discharge power for the SC at time *t*, kW. *Pmin sc,dis* and *Pmax sc,dis* are the minimum and maximum discharge power of the SC, kW. *SOCt sc* and *SOCt-1 sc* are the capacitance state of the SC at time *t* and the previous moment. *SOCmin sc* and *SOCmax sc* are the minimum and maximum capacitance state of the SC. $\eta_{sc,chr}$ and $\eta_{sc,dis}$ is the efficiency of charging and discharging for the SC.

### 2.2.3. Hydrogen energy systems(HESS)

(1) Electrolyzer (EL) [46]

The EL produces hydrogen by electrolyzing water. The EL chemistry works as follows:

$$H_2O \rightarrow O_2 + H_2$$

The EL produces hydrogen using electrical energy. At the same time, it also generates heat, and the working principle of the EL is shown in Eqs. (6)–(9):

$$P_{EL} = P_{EL\_H_2} + H_{EL} \tag{6}$$

$$P_{EL\_H_2} = P_{EL}\eta_{EL} \tag{7}$$

$$n_{EL\_H_2} = \eta_{EL} P_{EL\_H_2} \Big/ H_{H_2} M_{H_2} \tag{8}$$

$$Q_{EL} = H_{EL}\eta_{H_{EL}} \tag{9}$$

where, $P_{EL\_H2}$ is the amount of electricity used in hydrogen production for EL, kW. $H_{EL}$ is the heat of the EL during operation, kW. $\eta_{EL}$ is the power utilization efficiency of the EL. $H_{H2}$ is the calorific value of hydrogen, kJ/kg. $M_{H2}$ is the molar mass of hydrogen. $n_{EL\_H2}$ is The amount of substance that produces hydrogen for the EL, mol. $\eta_{HEL}$ is the efficiency of the use of heat generated for the EL.

The hydrogen production rate $v_{EL}$(mol/s) of the EL is calculated by Eq. (10). The input electrical power $P_{EL}$ of the EL is calculated by Eq. (12).

$$v_{EL} = \eta_F \frac{N_{EL} I_{EL}}{2F} \tag{10}$$

$$\eta_F = \frac{(I_{EL}/A_{EL})^2}{k_1 + (I_{EL}/A_{EL})^2} k_2 \tag{11}$$

$$P_{EL} = U_{EL} I_{EL} \tag{12}$$

where, $\eta_F$ is Faraday efficiency. $F$ is Faraday's constant. $k_1$ and $k_2$ is an empirical factor. $U_{EL}$ is the voltage of the EL, V. $I_{EL}$ is the current of the EL, A. $N_{EL}$ is the number of the EL in series. $A_{EL}$ is the effective electrode area of the EL, $m^2$.

(2) Fuel cell (FC)

The FC consumes hydrogen to output electricity and heat. It works as follows:

$$O_2 + H_2 \rightarrow H_2O$$

The FC produces electricity while hydrogen reacts with oxygen. At the same time, heat is generated, as shown in Eqs. (13)–(16) for the working principle of the FC:

$$P_{FC\_H_2} = n_{FC\_H_2} H_{H_2} M_{H_2} \Big/ \eta_{FC} \tag{13}$$

$$P_{FC} = P_{FC\_H_2} \Big/ \eta_{FC} \tag{14}$$

$$P_{FC} = P_{FC\_H_2} + H_{FC} \tag{15}$$

$$Q_{FC} = H_{FC}\eta_{H_{FC}} \tag{16}$$

where, $\eta_{FC}$ is the efficiency of the FC. $n_{FC\_H2}$ is the amount of hydrogen required for the FC, mol. $P_{EL\_H2}$ is amount of electricity needed to use hydrogen for the FC, kW. $H_{H2}$ is the calorific value of hydrogen, kJ/kg. $M_{H2}$ is the molar mass of hydrogen. $H_{FC}$ is the heat generated when the FC is working, kW. $\eta_{HFC}$ is the efficiency of the heat generated for the FC.

(3) Hydrogen storage tanks (HST)

The HST is used to compress and store hydrogen. The amount of the dynamic substance in the HST are expressed as:

$$n_{HST}(t+1) = n_{HST}(t) + v^{im}_{HST}(t)\Delta t - v^{ex}_{HST}(t)\Delta t \tag{17}$$

$$v^{im}_{HST}(t) = 3600 v_{EL}(t) \tag{18}$$

$$v^{ex}_{HST}(t) = 3600 v_{FC}(t) + v_{HST,HV}(t) \tag{19}$$

$$v^{im}_{HST}(t) v^{ex}_{HST}(t) = 0 \tag{20}$$

$$0 \le V_{HST} \le IC_{HST} \tag{21}$$

$$SOC_{HST}(t) = SOC_{HST}(t-1) + \frac{n_{HST}(t+1) - n_{HST}(t)}{n_{HST,max}} \tag{22}$$

where, *v*im HST and *v*ex HST are the hydrogen input and output rates of the HST, mol/h. $n_{HST}$(t + 1) is the amount of hydrogen stored in the HST at the next moment, mol. $n_{HST}$(t) is the amount of hydrogen stored in the HST at the moment, mol. $v_{FC}$(t) and $v_{EL}$(t) are hydrogen production and consumption rates of EL and FC, mol/s. $v_{HST,HV}$ is the hydrogen rate provided by the HST to the FC, mol/h. $V_{HST}$ is the capacity of stored hydrogen, $m^3$. $IC_{HST}$ is the installed capacity of the HST, $m^3$. Eq. (20) restricts the import and export of hydrogen at the same time and only one can be working. $SOC_{HST}$(t) and $SOC_{HST}$(t-1) are is the proportion of hydrogen stored in the HST at this moment and the previous moment relative to the rated capacity.

#### 2.2.4. Heat pumps(HP)

The HP converts electrical energy into heating or cooling energy, which is then transferred to a medium. It works as follows Eq. (23):

$$P^{(t)}_{HP} = P^{h(t)}_{HP} \Big/ \eta_{HP} \tag{23}$$

where, $P_{HP}$ is the input power of the HP, kW. *P*h HP is heating power for the output of the HP, kW. $\eta_{HP}$ is the efficiency of the HP.

#### 2.2.5. Storage tanks(WST)

WST is used as a storage of thermal energy, it can store both heat and cold. Its heat storage (*H*h/c WST*(t)*,kWh) and real-time state ($SOC_{WST}$) and constraints are calculated as follows:

$$H^{h/c}_{WST}(t+1) = H^{h/c}_{WST}(t)(1-\delta_{WST}) + \left( HP^{h/c,im}_{WST}(t)\eta^{im}_{WST} - \frac{HP^{h/c,ex}_{WST}(t)}{\eta^{ex}_{WST}} \right)\Delta t \tag{24}$$

$$SOC_{WST}(t) = \frac{H_{WST}(t)}{IC_{WST}} \tag{25}$$

$$SOC^{min}_{WST} \le SOC_{WST}(t) \le SOC^{max}_{WST} \tag{26}$$

where, $\delta_{WST}$ is the heat loss coefficient of the WST. $IC_{WST}$ is the installed capacity, kWh. *h/c* and *im/ex* represent heating/cooling and imported/exported energy. $H_{WST}$ is the thermal energy stored in the WST, kWh. $SOC_{WST}$ is the proportion of thermal energy stored in the WST relative to its rated capacity. $\eta_{WST}$ is the efficiency of storing or releasing thermal energy in the WST.

## 3. Methodology

Based on the model described in the previous section, this section will propose a collaborative optimization operation method for the system. First, the VMD technique is described in detail, which is used to decompose the source-load power difference into different frequency components (Section 3.1). Next, the operational logic for allocating each component to supercapacitors, hydrogen energy, and thermal storage systems is defined, respectively (Section 3.2). Third, a comprehensive set of cost assessment metrics is established for economic evaluation (Section 3.3). Finally, on this basis, three hierarchical operation strategies are developed—from fixed allocation benchmarks to adaptive, and then to grid-coordinated strategies (Section 3.4). The subsequent sections focus on the experimental validation of these control principles (Section 4) and their application and evaluation in full-scale simulation cases (Sections 5 and 6).

### 3.1. VMD crossover method

The VMD is a fully adaptive and non-recursive signal processing technique ideal for decomposing complex non-stationary signals such as the source-load differential power. Unlike Empirical Mode Decomposition (EMD), VMD proactively determines the relevant bands by solving a constrained variational problem.

The core of the VMD algorithm is to decompose a real-valued input signal $f(t)$ into a discrete number of sub-signals or modes $u_k(t)$, each having a specific sparsity property while reproducing the input signal. This is achieved by addressing the following constrained variational problem:

$$\min_{\{u_k\},\{\omega_k\}} \left\{ \sum_{k=1}^{K} \left\| \partial_t [(\delta(t) + j/\pi t) * uk(t)] e^{-j\omega_k t} \right\|_2^2 \right\} \tag{27}$$

$$\sum_{k=1}^{K} u_k(t) = f(t) \tag{28}$$

where, $\{u_k\} = \{u_1, u_2, u_3 \ldots u_K\}$ are the $K$ mode functions, $\{\omega_k\} = \{\omega_1, \omega_2, \omega_3 \ldots \omega_K\}$ are their corresponding center frequencies, $\delta$(t) is the Dirac delta function, * denotes convolution, and $\partial_t$ is the time derivative.

Variational model decomposition (VMD) decomposes and reconstructs the difference between PV power generation and load power. $k$ intrinsic mode functions (IMFs) are obtained by decomposing the differential power by VMD. They are shown in the following equation:

$$u_k(t) = A_k(t)\cos[\Phi_k(t)] \tag{29}$$

where, $u_k$ denotes the k-th modal component. $A_k$ denotes the amplitude of the k-th IMF. $\Phi_k$ indicates the phase.

The selection of the number of modes $K$ and the penalty parameter $\alpha$ is critical. In this study, the differential power signal was decomposed with different $K$ values. The value $K = 9$ was selected because it produced modes with distinct center frequencies without obvious mode mixing or redundant components, as based on spectral analysis from the resulting IMFs. The penalty parameter $\alpha$, which controls the bandwidth of each mode, was empirically set to 2000. This value was found to provide a good trade-off, ensuring that each mode captured a meaningful frequency component while avoiding excessive bandwidth that could lead to overlap. The distribution of the central frequencies of each component is shown in Fig. 3(a)–(c).

Spectrum analysis is performed on the $K$ IMFs obtained from VMD decomposition of the differential power to obtain their corresponding frequency components. The high-frequency component $P_H(t)$, the medium-frequency component $P_M(t)$ and the low-frequency component $P_L(t)$ are reconstructed according to the respective response characteristics of different energy storage devices. It is shown in the following equation:

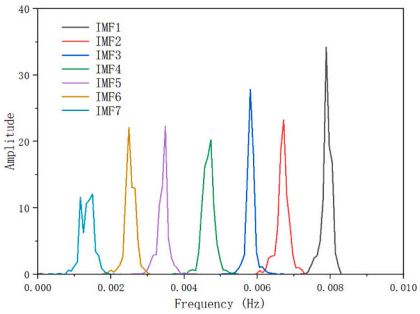


(a) Central frequency distribution diagram of IMF1-7

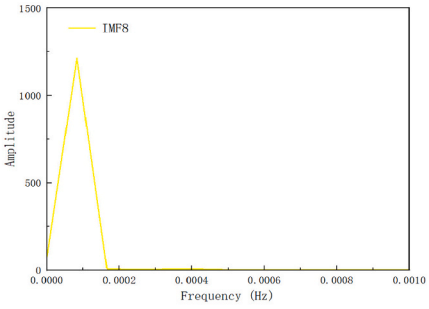


(b) Central frequency distribution diagram of IMF8

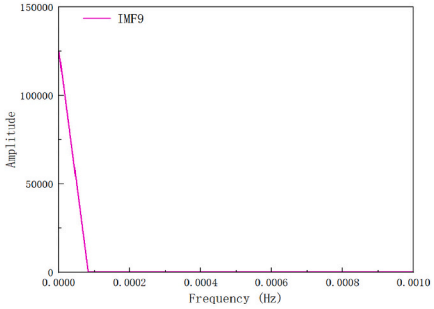


(c) Central frequency distribution diagram of IMF9

**Fig. 3.** Central frequency distribution of the IMFs.

$$P_{\mathrm{L}}(t)=\sum_{k=1}^{a}u_k(t)$$
$$P_{\mathrm{M}}(t)=\sum_{k=a+1}^{a+b}u_k(t) \tag{30}$$
$$P_{\mathrm{H}}(t)=\sum_{k=a+b+1}^{\mathrm{K}}u_k(t)$$

### 3.2. Multi-energy storage operation logic

As illustrated in Fig. 4, after the differential power generated between the PV and the load power undergoing frequency separation via the VMD method, the resulting components are allocated as follows: The low-frequency components are assigned to the thermal energy system. The mid-frequency components are allocated to the hydrogen energy system. The high-frequency components are directed to the operation of the SC system.

### 3.3. Cost evaluation indicators

The operating costs of PV are shown in the following equation:

$$C_{\mathrm{PV}}=P_{\mathrm{PV}}S_{\mathrm{PV}} \tag{31}$$

where, $S_{\mathrm{PV}}$ is the unit price of 1 kW for PV operation.

The operating costs of HESS are shown in the following equation:

$$C_{\mathrm{HESS}}=P_{\mathrm{EL}}S_{\mathrm{charge}}+P_{\mathrm{FC}}S_{\mathrm{discharge}}+n_{\mathrm{HST}}N_{\mathrm{HST}}+I_{\mathrm{HESS}}/N_{\mathrm{HESS}} \tag{32}$$

where, $S_{\mathrm{charge}}$ and $S_{\mathrm{discharge}}$ are unit price of 1 kW for the EL and FC running. $S_{\mathrm{HST}}$ is the unit price of 1 kg for the operation of the HST. $I_{\mathrm{HESS}}$ is the construction cost of hydrogen energy systems. $N_{\mathrm{HESS}}$ is the service life of the hydrogen energy system. $N_{\mathrm{HST}}$ is the cost of storing 1 mol of hydrogen for a HESS. $n_{\mathrm{HST}}$ is the amount of hydrogen stored in the HST, mol.

The operating cost of SC is shown in the following equation:

$$C_{\mathrm{SC}}=P_{\mathrm{sc\_charge}}S_{\mathrm{sc\_charge}}+P_{\mathrm{sc\_discharge}}S_{\mathrm{sc\_discharge}}+I_{\mathrm{sc}}/N_{\mathrm{sc}} \tag{33}$$

where, $S_{\mathrm{sc\_discharge}}$ and $S_{\mathrm{sc\_charge}}$ are the unit price of 1 kW for SC discharging and discharging. $I_{\mathrm{sc}}$ is the construction cost of SC. $N_{\mathrm{sc}}$ is the service life of the SC.

The operating costs of the thermal energy system are shown in the following equation:

$$C_{\mathrm{heat}}=P_{\mathrm{HP}}S_{\mathrm{HP}}+P_{\mathrm{WST}}S_{\mathrm{WST}}+I_{\mathrm{HPSS}}/N_{HPSS} \tag{34}$$

where, $S_{\mathrm{HP}}$ is the unit price of 1 kW for the operation of the HP. $S_{\mathrm{WST}}$ is the unit price of 1 kJ stored in a WST tank for heat. $I_{\mathrm{heat}}$ is the cost of construction of HP systems. $N_{\mathrm{heat}}$ is the service life of the thermal energy system.

The cost of municipal grid participation is shown in the following equation:

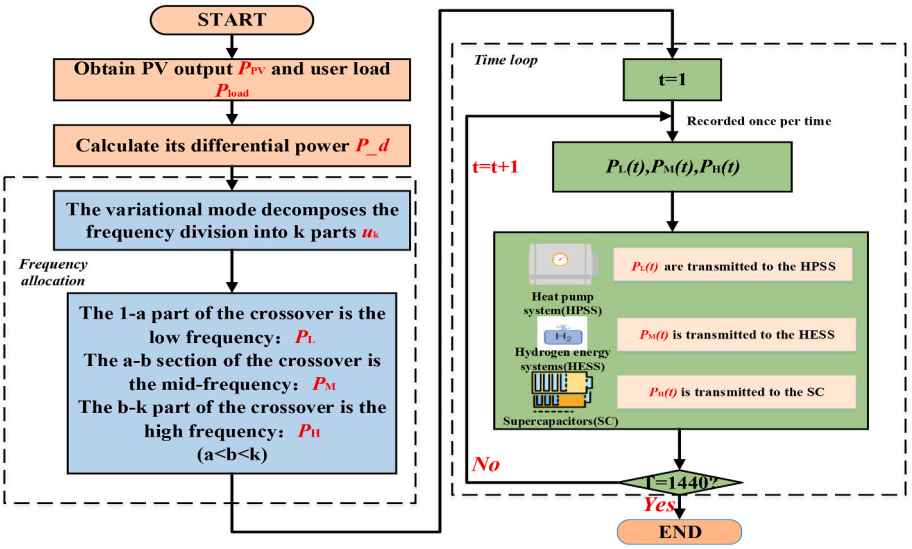


**Fig. 4.** Working principle of the VMD-based power allocation.

$$C_{\text{grid}} = P^{im}_{\text{grid}} S^{im}_{\text{grid}} - P^{ex}_{\text{grid}} S^{ex}_{\text{grid}} \tag{35}$$

where, *P*im grid and *P*ex grid indicate that the system supplied power to the grid and the grid supplied power to the system, kW. *S*im grid and *S*ex grid indicate the unit price of power purchase from the grid and system sale electricity to the grid.

The above five parts are calculated as the running cost of a time node $t$ (1 min). The total running cost is as follows:

$$C_{\text{PV\_total}} = \sum_{t=1}^{\text{T}} C_{\text{PV}}(t) \tag{36}$$

$$C_{\text{HESS\_total}} = \sum_{t=1}^{\text{T}} C_{\text{HESS}}(t) \tag{37}$$

$$C_{\text{SC\_total}} = \sum_{t=1}^{\text{T}} C_{\text{SC}}(t) \tag{38}$$

$$C_{\text{heat\_total}} = \sum_{t=1}^{\text{T}} C_{\text{heat}}(t) \tag{39}$$

$$C_{\text{grid\_total}} = \sum_{t=1}^{\text{T}} C_{\text{grid}}(t) \tag{40}$$

$$C_{\text{total}} = C_{\text{PV\_total}} + C_{\text{HESS\_total}} + C_{\text{SC\_total}} + C_{\text{heat\_total}} + C_{\text{grid\_total}} \tag{41}$$

where, $T$ is the number of minutes in 1 day, i.e. 1440 min.

To evaluate the utilization of energy storage capacity, the maximum Excess Capacity Ratio (ECR) is calculated as follows:

$$ECR = \max\left(D_{\text{exceed\_max},i} / D_{\max}\right) \tag{42}$$

Among it, the $D_{\text{exceed\_max,i}}$ is the maximum amount of electricity/hydrogen/heat that each energy storage device cannot store during the operation of the strategy, kg or kJ or mol. $D_{\max}$ is the rated capacity of each energy storage device, kg or kJ or mol. A lower ECR indicates a higher utilization of the installed storage capacity and less energy waste.

### 3.4. Three running strategies in the system

After establishing the system model, we developed a hierarchical, rule-based optimization framework composed of three sequentially refined control strategies, each building upon the previous one to achieve progressive system-level refinement:

(1) Strategy 1: main power allocation

Based on VMD, the power difference is first decomposed into different frequency components and directly allocated to the corresponding subsystems. This basic strategy establishes a benchmark power distribution and provides preliminary optimization results.

(2) Strategy 2: SOC-adaptive VMD tuning

Building on the output of Strategy 1, this stage introduces real-time adjustments of the three VMD crossover parameters in response to the State of Charge (SOC) of the energy storage system. This allows for dynamic fine-tuning of power allocation, effectively reallocating power components between the SC, HESS, and thermal system, enhancing system adaptability.

(3) Strategy 3: grid-assisted frequency ratio adjustment

Further refining Strategy 2, this layer incorporates interactions with the municipal grid and dynamically adjusts the frequency-based power allocation ratio based on SOC feedback. This ensures effective energy storage regulation and further overall system optimization, while keeping all storage units within safe operational limits.

## 4. Experimental verification

In order to verify the effectiveness of the strategy proposed in the previous section, this section will introduce the validation work based on a scaled-down experimental platform.

### 4.1. Introduction to the test bench

The experimental system is illustrated in Fig. 5. The test bench comprises photovoltaic equipment, lithium iron phosphate battery, supercapacitor and load equipment. Each device is regulated by the central controller.

This experimental equipment setup utilizes the difference power as the primary input data which is between the output power of photovoltaic($P_{\text{PV}}$) and load demand power($P_{\text{load}}$). The difference between photovoltaic power and load power is obtained as the required data. The calculation equation is as follows:

$$P_{\text{net}} = P_{\text{PV}} - P_{\text{load}} \tag{43}$$

The low-pass filtering algorithm decomposes the differential power $P_{\text{net}}$ into two frequencies, high frequency and low frequency. The high-frequency components of power will be allocated to the supercapacitor, while the low-frequency power will be assigned to the lithium iron phosphate battery.

It should be noted that this experimental platform is a scaled-down, electricity-focused prototype centered on electric energy, designed to verify the feasibility of the control strategy. Its primary objective is to check the correctness and real-time performance of the control logic proposed in Section 3: 'VMD frequency decomposition - power allocation - SOC real-time adjustment - grid coordination. Furthermore, since the hydrogen and thermal systems in the full model primarily interact with the electrical bus through power conversion, the lithium battery in the experimental platform can effectively emulate their aggregate power regulation role for the purpose of validating the core control strategy.

Therefore, the case studies in Sections 5 and 6 essentially combine the experimentally validated control algorithm with hydrogen/thermal device models based on physical principles and literature data to evaluate the performance of the complete system in simulation.

### 4.2. Frequency divider verification under source-charge power changes (strategy 1)

#### 4.2.1. Analysis of PV power fluctuation results

The photovoltaic output power was varied by partially shielding the panels, while the load demand power was held constant. Under this condition, the differential power in this scenario only changes with the change of photovoltaic power. The photovoltaic output power and load demand power are shown in Figs. 6 and 7.

As shown in Fig. 7, the photovoltaic output power changed significantly every 30–50 s. In contrast, the load demand stably operated on the load side from 0 s to 300 s and from 300 s to 600 s.

Fig. 8 illustrates the differential power and the operational status of the supercapacitor and lithium iron phosphate battery.

Whenever the PV output power changed, the supercapacitor immediately responded to the high-frequency power. Its output power initially matched the change in differential power and then gradually decreased over time. Conversely, the lithium iron phosphate battery increased its output power over time. Eventually it reached the same level as the differential power.

#### 4.2.2. Analysis of load power fluctuation results

In contrast to the previous experiment, this experiment adjusted the load demand by stepping it up or down at each step. The differential power varied solely with changes in the load demand. The PV output power and the load demand power are presented in Figs. 9 and 10. Fig. 11 illustrates the variations in differential power and the

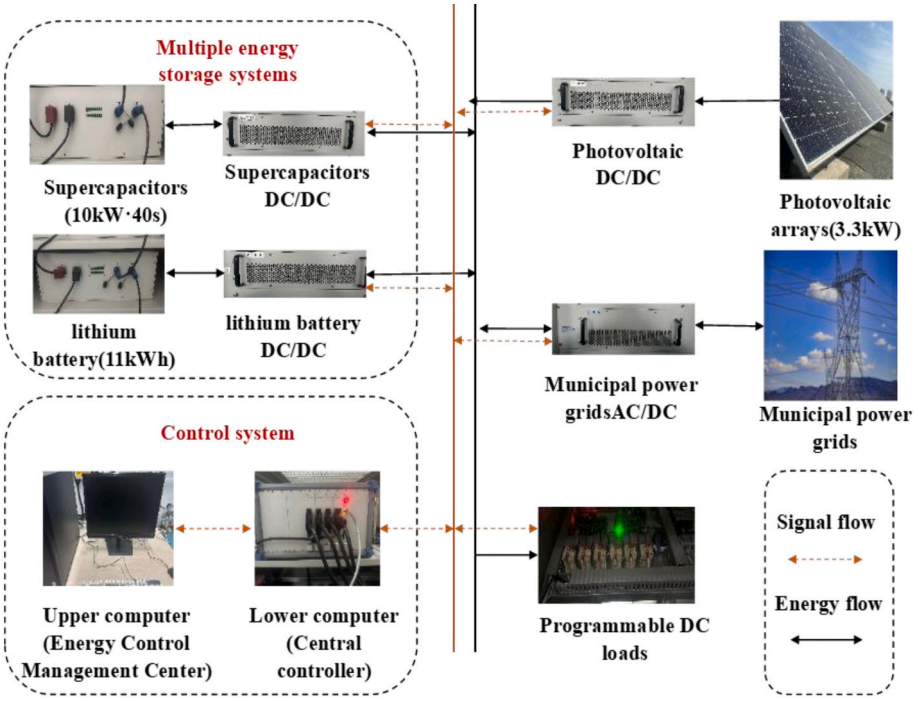


**Fig. 5.** Schematic of the experimental platform.

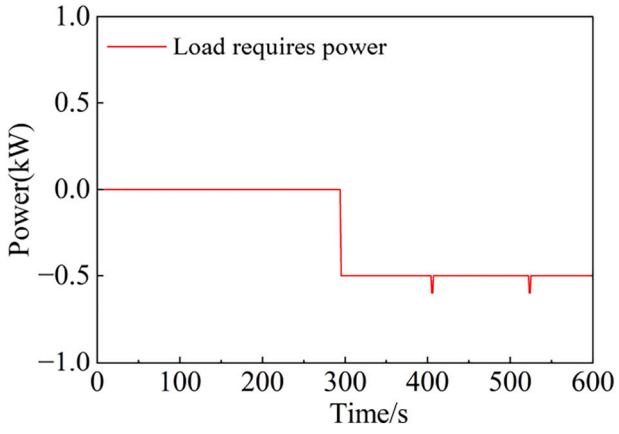


**Fig. 6.** Load demand power.

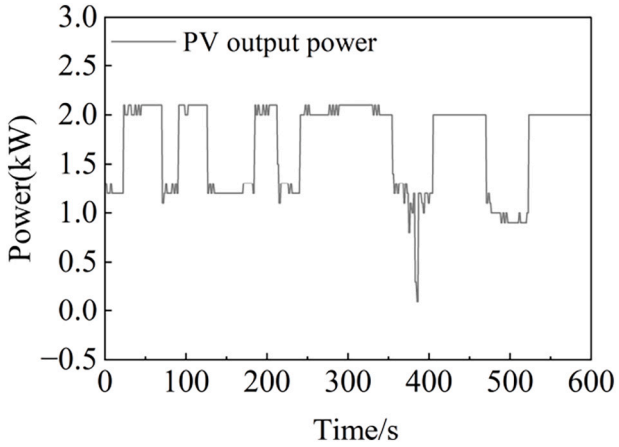


**Fig. 7.** Photovoltaic output power.

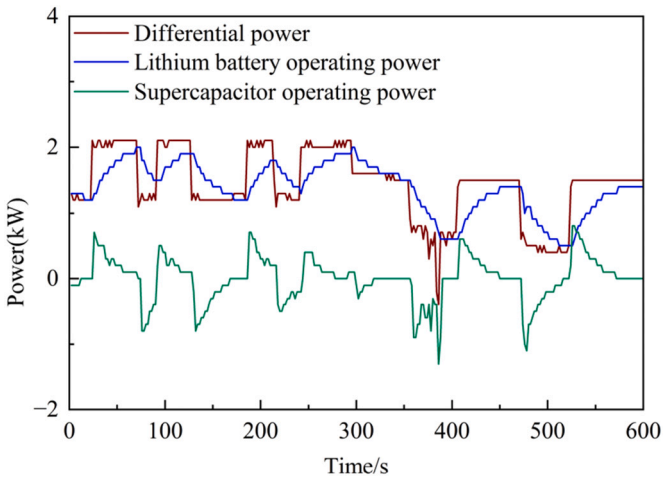


**Fig. 8.** Differential power and the operating status of supercapacitors and lithium iron phosphate batteries.

corresponding operation states of the supercapacitor and lithium iron phosphate battery.

Whenever the load demand power changes, the change trend of the supercapacitor and lithium iron phosphate battery is consistent with the previous experiment, so it is not mentioned here. This experiment verified the feasibility of power allocation from the load side.

### *4.3. SOC-aware crossover power adjustment (strategy 2)*

To verify that the power at each frequency could be effectively regulated after frequency division, the filter constant (*fc*) was adjusted based on the real-time state of the supercapacitor. The real-time operating power of the lithium iron phosphate battery and supercapacitor was observed during fluctuations in the differential power.

In this section, the load power and the *fc* were adjusted for the experiment. The state of charge (SOC) of the supercapacitor ranged from

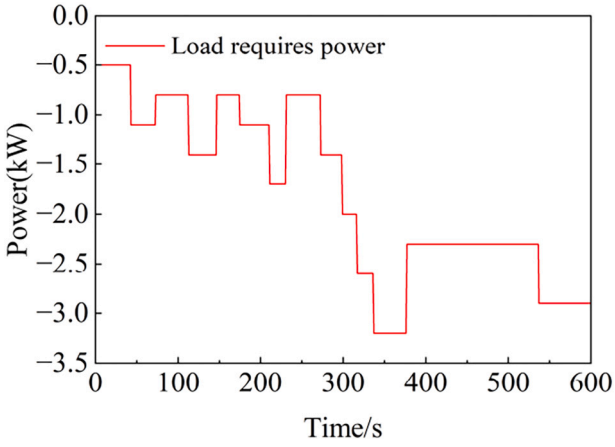


**Fig. 9.** Load demand power.

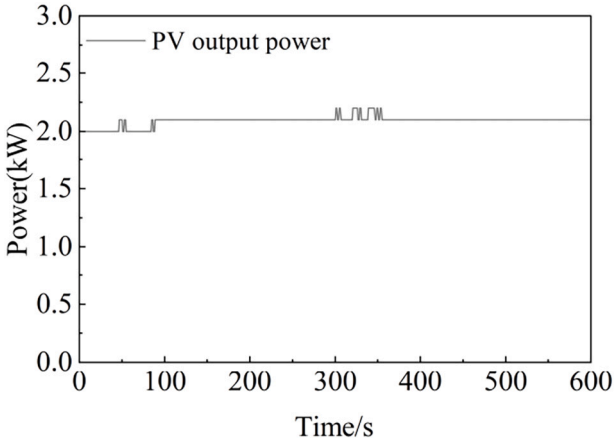


**Fig. 10.** Photovoltaic output power.

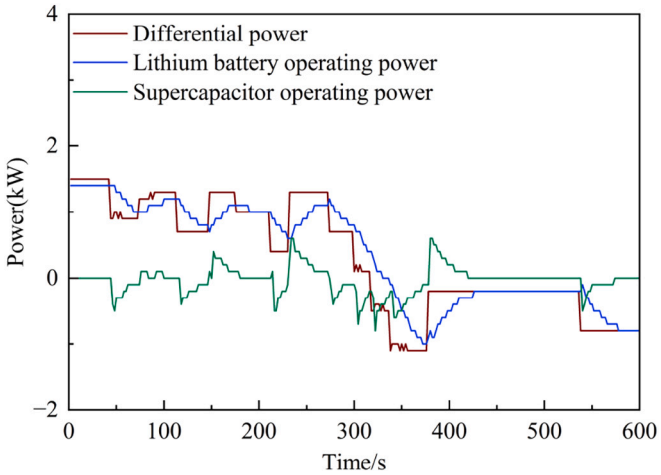


**Fig. 11.** Differential power and the operating status of supercapacitors and lithium iron phosphate batteries.

excessively low to excessively high. When the SOC of the supercapacitor was too low, the high-frequency component increased, while the low-frequency component decreased. Conversely, when the SOC was too high, the high-frequency component decreased, while the low-frequency component increased.

Therefore, this experiment was analyzed separately for two scenarios.

#### 4.3.1. *The SOC of the supercapacitor is too high*

As shown in Fig. 11, the experiment was divided into two phases. During the first phase (0 to 200 s), the *fc* was set to a higher than normal state. It led to reduce the high-frequency power. During the second phase (200 to 500 s), the *fc* was set to the normal state.

The experimental results are shown in Fig. 12. In the first 200 s, when the SOC of the supercapacitor was high, the operating power of the supercapacitor was lower than under normal conditions. It effectively reduced the energy stored in the supercapacitor. After resetting the SOC of the supercapacitor, the supercapacitor returned to normal operation after 200 s. There was no difference with normal conditions.

#### 4.3.2. *The SOC of the supercapacitor is too low*

As shown in Fig. 13, in the initial phase (0 to 150 s), the *fc* is set the same as in section 4.3.1 for 200–500 s. From 150 to 500 s, the *fc* was set to a lower than normal state, resulting in an increase in high-frequency power.

The experimental results are shown in the Fig. 13. Whenever the load demand power changes, the change trend of the supercapacitor and lithium iron phosphate battery is consistent with the previous experiment, so it is not mentioned here. However, because the filtering constant became smaller, the power dynamics of each device changed more slowly. The response time increased as well. After 400 s, the supercapacitor had reached its rated power, and the experimental strategy was concluded.

The two experiments in this section successfully verified the feasibility of real-time power allocation of multiple energy storage devices.

### 4.4. *Consider verification of grid-connected frequency divider (strategy 3)*

To verify that the power at each frequency could be appropriately adjusted in real time based on conditions after frequency division, the real-time state of the supercapacitor and the lithium battery was used as the criterion. Grid power was introduced to regulate the operating conditions of the energy storage devices. The real-time operating power changes of the lithium iron phosphate battery and the supercapacitor were observed during fluctuations in the differential power.

Consisting with the experiment in Section 4.2, the differential power was regulated through adjustments in either load demand power or photovoltaic output power. However, when supercapacitors and lithium-ion batteries reached specific operational thresholds (e.g., state-of-charge limits), they ceased charging/discharging operations. Instead, it use the power grid to compensate for power imbalances.

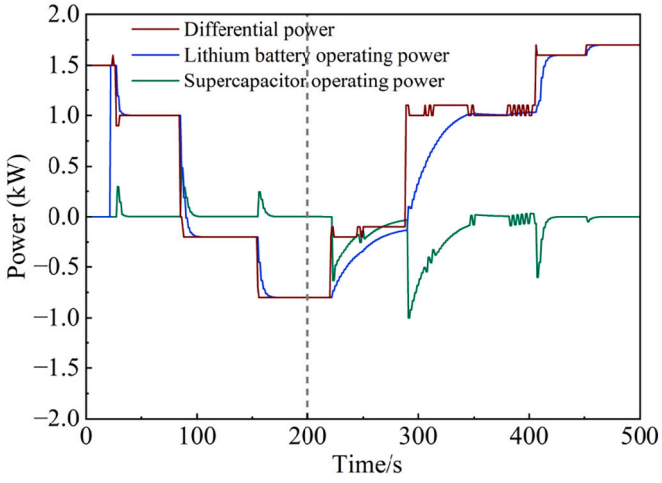


**Fig. 12.** Experiment running under the condition that the supercapacitor SOC was too high.

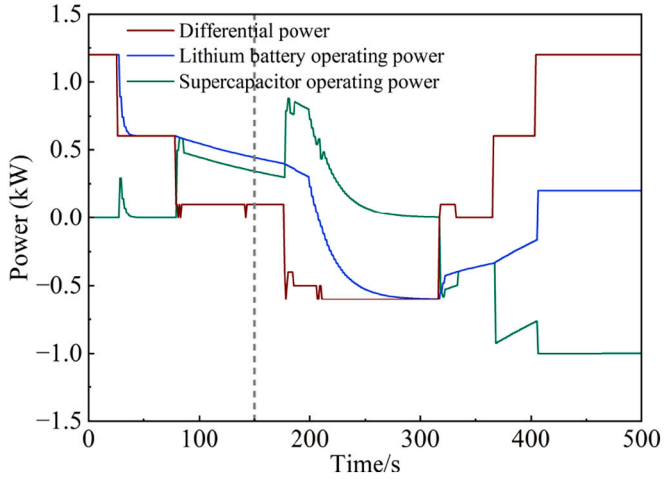


**Fig. 13.** Experiment running under the condition that the SOC of the supercapacitor was too low.

Therefore, four scenarios were designed to test the SOC of the supercapacitor and the battery.

*4.4.1. Taking the SOC of supercapacitor as an example*

(1) When the SOC of the supercapacitor is too high

When the SOC of the supercapacitor is too high, the power operation curves of the supercapacitor and the lithium battery are shown in Fig. 14.

When the SOC of the supercapacitor exceeded the predefined threshold, the charging mode was disabled. The experimental results are shown in the Fig. 14. From 0 to 280 s, the supercapacitor operated normally. This is the same as described in Section 4.2. From 280 to 600 s, the supercapacitor was unable to operate normally so that the utility grid assumed its role. The behavior of the grid mirrored the supercapacitor. This result aligned with the expected experimental results.

Due to limitations of the experimental platform, the supercapacitor exhibited a response delay of 3–5 s following changes in differential power. Consequently, the utility grid provided power during this initial delay before the supercapacitor resumed operation. This behavior was consistent across all experiments in this section. Therefore, it is not reiterated in subsequent parts.

(2) When the SOC of the supercapacitor is too low

When the SOC of the supercapacitor is too low, the power operation curve of the supercapacitor and the lithium battery is shown in the following Fig. 15:

When the SOC of the supercapacitor fell below the predefined threshold, the discharge mode was disabled. The experimental results are shown in Fig. 15. From 0 to 250 s, the differential power gap gradually increased. The supercapacitor was unable to operate normally. The municipal power grid replaced the supercapacitor to operate. The behavior of the grid mirrored the supercapacitor. From 250 to 350 s, the supercapacitor operated normally. This is the same as described in Section 4.2.

*4.4.2. Take lithium battery SOC as an example*

(1) When the SOC of the battery is too high

When the SOC of the lithium battery is too high, the power operation curve of the differential power, supercapacitor and lithium battery is shown in the following Fig. 16:

When the SOC of the lithium battery exceeded the predefined threshold, the charging mode was disabled. The experimental results are shown in the Fig. 16. From 0 to 30 s and from 340 to 450 s, the differential power was positive. During these periods, the lithium battery was unable to store energy. The municipal grid received the power that would otherwise have been stored by the battery. The behavior of the grid mirrored the lithium battery which was under normal conditions. From 30 to 340 s, the lithium battery operated normally. This is the same as described in Section 4.2.

(2) When the SOC of the battery is too low

When the SOC of the lithium battery is too low, the power operation curve of the differential power, supercapacitor and lithium battery is shown in the following Fig. 17:

When the SOC of the lithium battery fell below the predefined threshold, the discharging mode was disabled. The experimental results are shown in the Fig. 17. From 0 to 170 s and from 330 to 450 s, the lithium battery operated normally. This is the same as described in Section 4.2. From 170 to 330 s, the lithium battery was unable to store energy. The utility grid assumed its role, operating in a manner consistent with the lithium battery under normal conditions. These results aligned with the expected behavior and confirmed the effectiveness of the proposed strategy.

*4.5. Simulation and experimental data comparison*

The validation process is crucial to ensure the simulation model reliably represents the physical system's behavior. Under the condition that the initial data (photovoltaic output and load demand) remained unchanged, the experimental strategies described in the previous three sections were implemented by using MATLAB software. The simulation

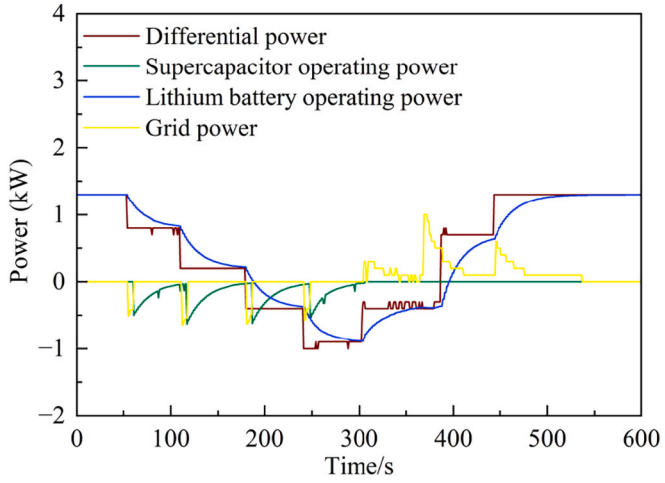


**Fig. 14.** When the SOC of a supercapacitor is too high, the operating curve of each device.

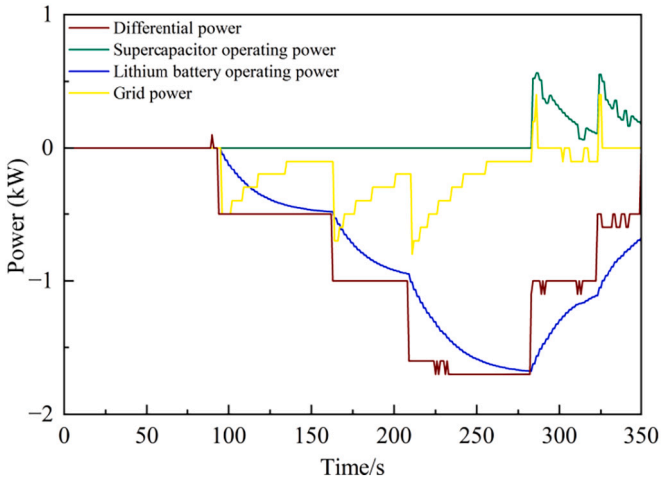


**Fig. 15.** When the SOC of a supercapacitor is too low, the operating curve of each device.

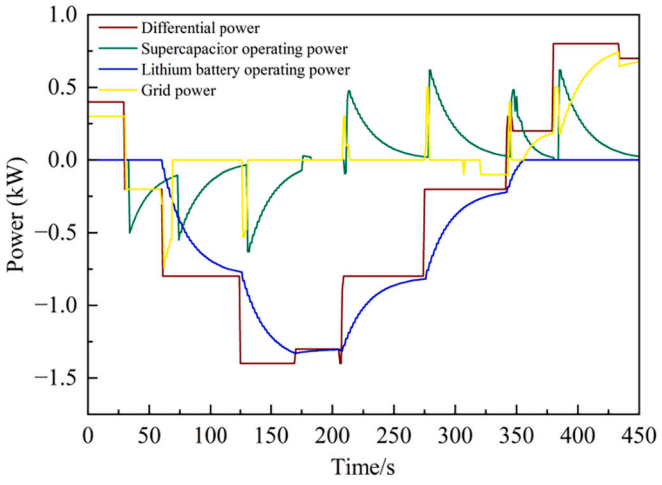


**Fig. 16.** When the SOC of a lithium battery is too high, the operating curve of each device.

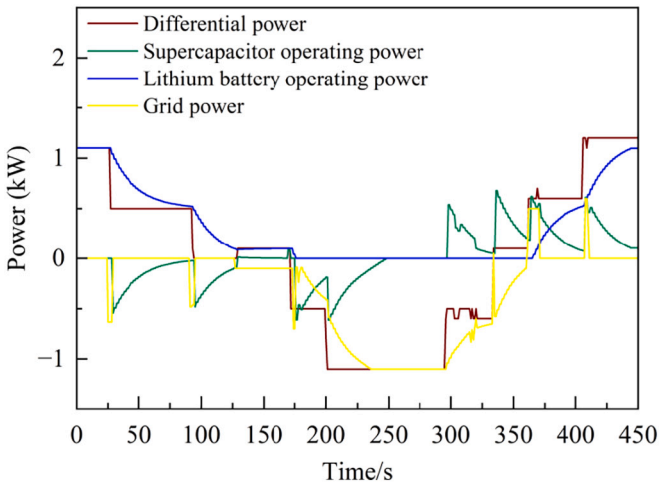


**Fig. 17.** When the SOC of a lithium battery is too low, the operating curve of each device.

results are shown in Fig. 18.

The simulation results showed a high degree of consistency with the experimental results. However, the response speed of each device appeared faster and the power operation of the equipment were more flexible in the simulation. This discrepancy was because the simulation did not account for the short delays in the response of the physical equipment, which are inherent in real-world systems. The experimental results demonstrated the feasibility and reliability of the three frequency division methods. It was evidenced by their effective management of power distribution under varying load conditions.

To quantitatively validate the accuracy of the simulation model, statistical error metrics including Root Mean Square Error (RMSE) and Mean Absolute Error (MAE) were calculated by comparing the experimental and simulated values of three critical operational parameters: the differential power (P_net), supercapacitor power (P_sc), and lithium iron phosphate battery power (P_bat). The results are summarized in Table 2.

The analysis results indicate that the RMSE and MAE values of all key variables are below 0.21 kW. Considering that the power level of the experimental system is in the kilowatt range, the absolute error level is extremely low. This result statistically confirms the high consistency between the simulation model and the physical experimental platform, providing a strong quantitative basis for the accuracy of the model's dynamic response.

After this section's experiment verified the feasibility of the control core logic, Sections 5–6 will apply the validated strategy to a complete community case including hydrogen/thermal systems for simulation studies.

## 5. Case settings

### 5.1. Source and load energy situation

This study focuses on the operation of a photovoltaic integrated energy system with multiple energy storage systems. The proposed system is applied to a case study of a residential community in Beijing. The system was simulated using MATLAB for a typical winter day based on the measured data for rooftop photovoltaic irradiance. The sampling interval was 1 min. The solar photovoltaic output and the electric and heating load of the community are shown in Figs. 19 and 20.

According to Eq. (43), the differential power of the system is obtained as shown in Fig. 21.

After VMD, the differential power is decomposed into 9 intrinsic mode functions (IMFs), as shown in Fig. 22. Therefore, IMF1-2 are grouped as high-frequency components (as shown in Fig. 23(a)). The mid-frequency band, represented by IMF3–6, contains more complex frequency components, which require detailed decomposition (as shown in Fig. 23(b)). IMF7-9, with the lowest center frequencies, are suitable for energy storage devices with slower response characteristics and are grouped as low-frequency components (as shown in Fig. 23(c)). This grouping allows for the utilization of different energy storage devices based on their response characteristics.

### 5.2. Economic-technical parameters

Table 3 shows the relevant parameters of each equipment in this system.

### 5.3. Analysis of system efficiency and dynamic performance

Based on the equipment model established in Section 2.2 and the experimental verification results in Section 4, this section deeply analyzes the overall energy efficiency and dynamic performance of the system under the proposed control strategy.

System energy conversion efficiency is an important index to evaluate the performance of multi-energy system. In this paper, the conversion efficiency of key energy links is quantitatively analyzed: the round-trip efficiency of electricity-hydrogen-electricity is $\eta_{EL}{}^{*}\eta_{EL} = 0.6{*}0.6 = 0.36$, which indicates that there is a significant conversion loss in the process of realizing deep energy time shift. In contrast, the thermal system shows high energy utilization efficiency, and the heating energy efficiency ratio of the HP $\eta_{HP}$ reaches 0.98. At the same time, the system makes full use of the waste heat generated during the operation of the FC and the electrolytic cell. The economic advantage of strategy 3 partly stems from its ability to optimally schedule energy links with different efficiencies: by introducing power grid to participate in real-time regulation, this strategy effectively reduces the number of high-cost hydrogen energy cycle conversion, and allocates more energy scheduling tasks to high-efficiency or low-cost links (such as power grid interaction and direct heating), thus improving the overall energy economy at the system level.

The dynamic stability of the system is crucial for integrating a high proportion of volatile renewable energy. The experimental results in Section 4 show that the hierarchical control strategy proposed in this paper can maintain the real-time power balance of the system under the second-to-minute timescale power fluctuations, which verifies its good primary frequency response ability. Specifically, the instantaneous response of SCs to high-frequency power components and the smooth compensation of low-frequency components by lithium batteries are effectively complementary. This coordinated control mechanism based

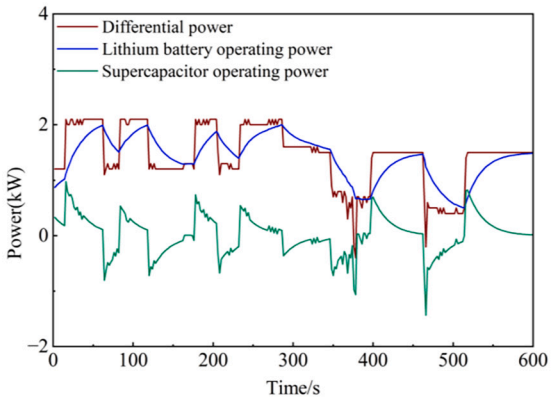


(a)Differential power under photovoltaic variation with simulated operation of supercapacitors and lithium iron phosphate batteries (Experiment 4.2.1)

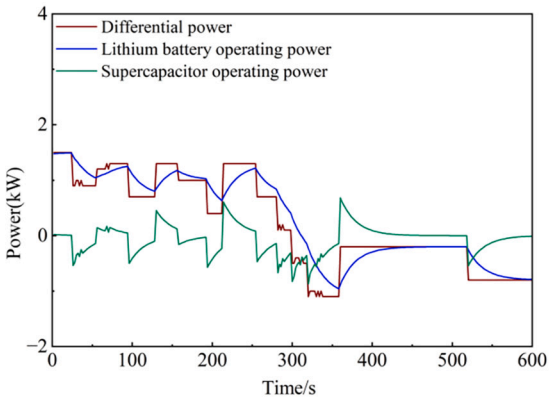


(b)Conform to the simulation of differential power under variation with supercapacitors and lithium iron phosphate batteries (Experiment 4.2.2)

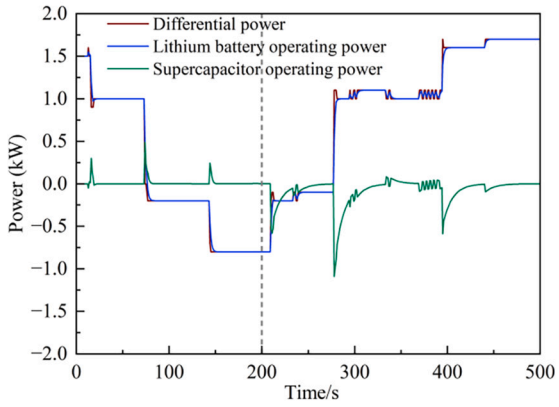


(c)Simulation results under the condition that the supercapacitor SOC is too high (Experiment 4.3.1)

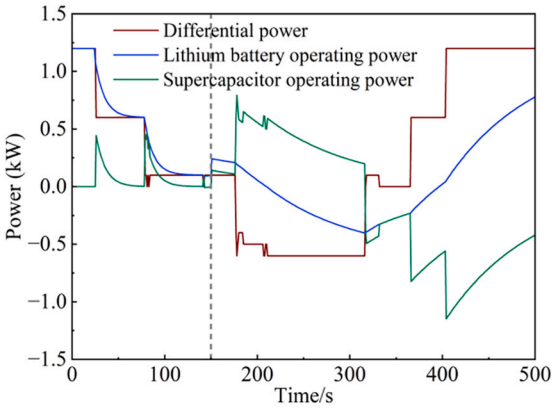


(d)Simulation results under the condition that the supercapacitor SOC is too low (Experiment 4.3.2)

**Fig. 18.** Simulation results for each experiment.

on VMD frequency domain decomposition constitutes the core foundation for the dynamic and stable operation of the system.

## 6. Results and discussion

In this section, the three frequency division strategies introduced in Section 3.4 are applied to a case study in a residential area in Beijing. The feasibility of these strategies are analyzed.

### 6.1. Normal operation characteristics analysis (strategy 1)

Based on the system model described in Section 2 and the VMD method detailed in Section 3.1, the energy storage and release profiles, as well as the SOC of WSTs, SCs, HSTs, at 1-min intervals over a 24-h period were shown in Fig. 24(a), (b), (c).

Fig. 24(a) illustrates the operation of the SC over a typical day. The SC operated from 6:00 to 18:00, handling high-frequency power due to significant residential load and strong fluctuations during this period. This period of significant residential activity and the peak of solar irradiance, as seen in Fig. 19, where both load and PV power exhibit high variability, necessitating high-frequency power support from the SC.

Fig. 24(b) shows the operation of the HST over a typical day. It bore a large amount of intermediate frequency load. During the 8:00–16:00 period, the HST was in the state of hydrogen storage. From 16:00 to 24:00, the HST was in the state of hydrogen release. This transition corresponds to the decline in photovoltaic power generation after 16:00 (Fig. 19) and the subsequent increase in nighttime electricity demand, which requires the HESS to switch from storage mode to power generation mode.

Fig. 24(c) shows the operational characteristics of the thermal WST during a typical day. The WST operated from 05:00 to 24:00. During the

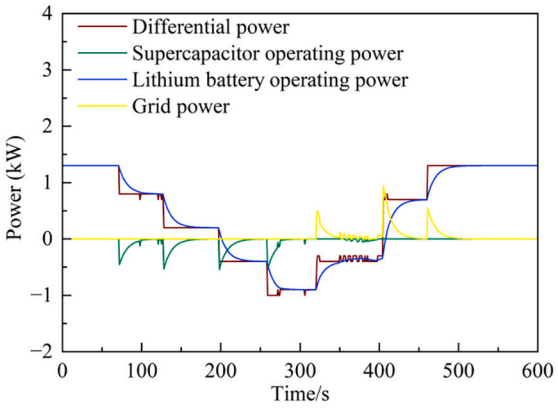


(e)When the SOC of a supercapacitor is too high, the analog operating curve for each device (Experiment 4.4.1(1))

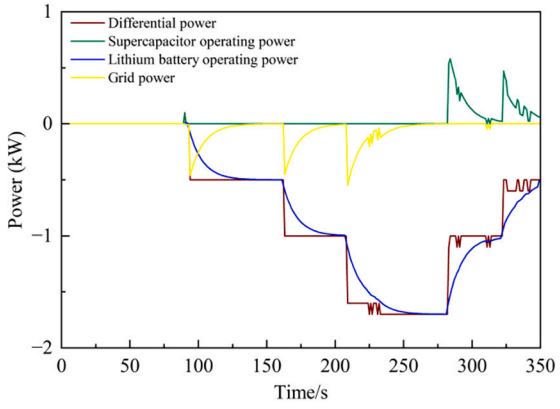


(f)When the SOC of a supercapacitor is too low, the analog operating curve for each device (Experiment 4.4.1(2))

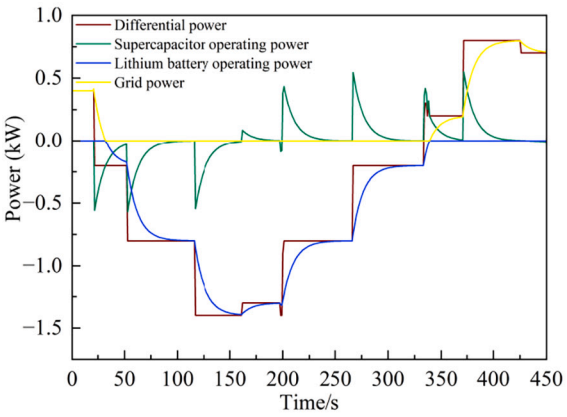


(g)Analog operating curves for each device when the SOC of a lithium battery is too high (Experiment 4.4.2(1))

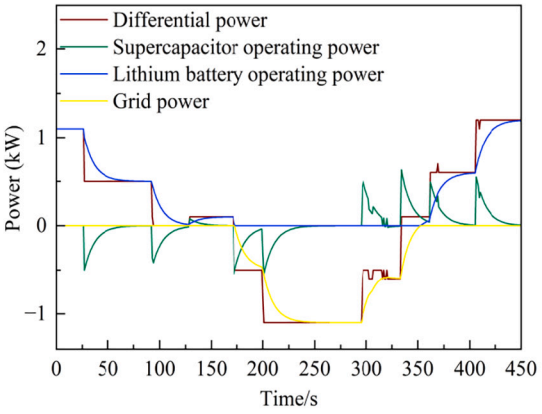


(h)Analog operating curves for each device when the SOC of a lithium battery is too low (Experiment 4.4.2(2))

**Fig. 18.** (*continued*).

**Table 2**
Statistical error metrics between experimental and simulated data.

| Variable | RMSE (kW) | MAE (kW) |
|---|---|---|
| Differential Power (P_net) | 0.18 | 0.12 |
| Supercapacitor Power (P_sc) | 0.15 | 0.10 |
| Battery Power (P_bat) | 0.21 | 0.14 |

periods of 05:02–09:00 and 15:58–23:00, the WST was in an exothermic state, releasing heat to meet demand. Conversely, from 07:30 to 14:18, the WST operated in a heat storage state, effectively contributing to peak shaving and valley filling. From 14:18 to 15:57, the WST reached its maximum storage capacity. Its excess heat is discarded due to system limitations.

### 6.2. Crossover power ratio adjustment analysis (strategy 2)

Based on the VMD frequency decomposition method described in Section 6.1, the proportions of the three frequency components are dynamically adjusted according to the real-time SOC of the energy storage device. Under this strategy, the system is simulated again. This is achieved by setting a control method that adjusts the boundary frequencies in the VMD output. For example, when the SOC of the SC is low, the controller effectively increases the bandwidth classified as 'high frequency,' directing more power to charge the SC, and vice versa.

Fig. 25(a), (b), (c) show the system operation diagram obtained after 24 h of operation.

Fig. 25(a) illustrates the performance curve of the SC on a typical day under Strategy 2. However, after 13:20, the SC received a portion of the intermediate frequency component, leading to a significant divergence in its operation compared to Strategy 1. During this period, the SOC reduction rate of the SC slowed down. After 20:20, the SC was further influenced by the HESS, which distributed a portion of the high-frequency components to the HESS.

Fig. 25(b) depicts the operation curve of the HST on a typical day under Strategy 2. Although the HESS was influenced by the SC and HP system, the operational trend of the HST in Strategy 2 remained consistent with that in Strategy 1. Therefore, detailed analysis was

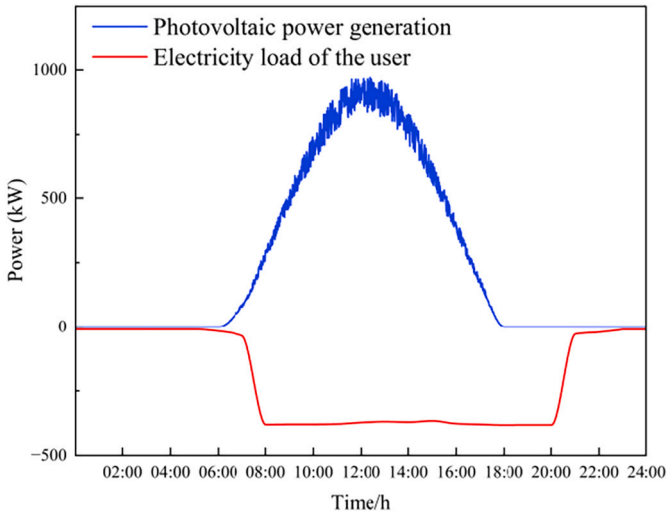


**Fig. 19.** Photovoltaic power supply and user electricity load.

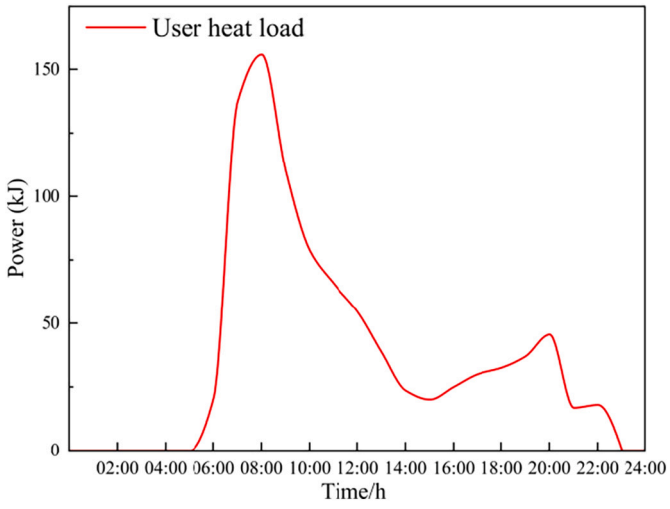


**Fig. 20.** User's heat load.

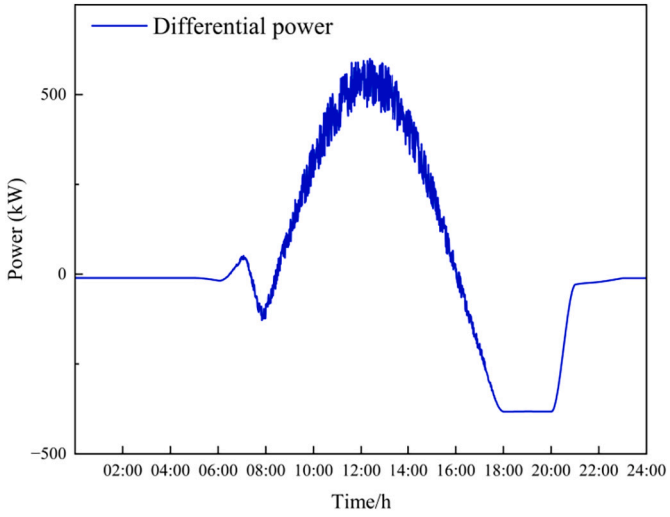


**Fig. 21.** Differential power.

omitted here.

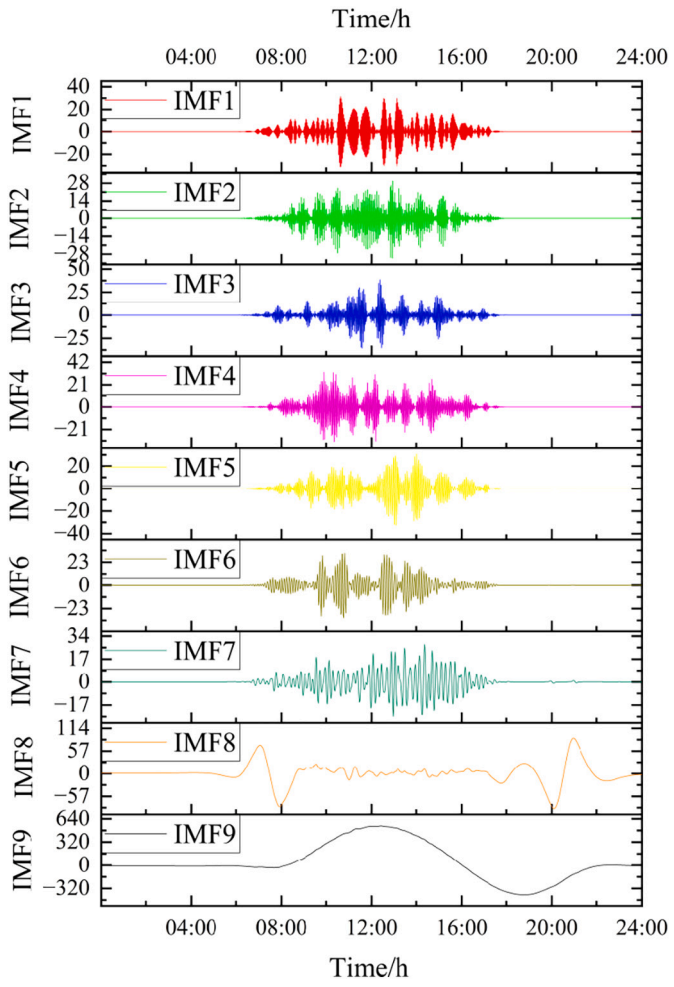


**Fig. 22.** Frequency division of each component.

Fig. 25(c) presents the operating curve of the WST over a typical day. The operation of the WST from 8:20 to 9:40 and from 13:20 to 16:00 differed significantly from that under Strategy 1. Starting from 8:20 a.m., the SOC of the WST is already below 0.15. The HP system was supplemented by some of the intermediate frequency components. After 13:20, the SOC of the WST has reached 0.7, and the HESS was also supplemented by some low-frequency components.

### *6.3. Grid integration analysis (strategy 3)*

Building on Strategy 2, the municipal power grid is integrated to jointly provide or recover the required electrical energy when the SOC of the SC or the WST exceeds its operational limits. This collaborative approach between the municipal grid and the HESS ensures efficient energy replenishment and adjustment. Under this strategy, the system is re-simulated for operation.

Fig. 26(a), (b), (c), (d) shows the system operation diagram obtained after 24 h of operation.

Fig. 26(a) presents the typical daily operational curve of a SC under Strategy 3. With the integration of the municipal grid, the SC was charged by the municipal grid at 13:09, 14:05 and 16:07. This demonstrated the grid's role in stabilizing SC operation and optimizing energy storage utilization.

Fig. 26(b) depicts the daily operation of a HST under Strategy 3. The operation of the HST was influenced by the SC and HP systems. Under this strategy, the hydrogen releasing by power generation increased. This highlighted the synergistic interaction between different energy storage components in the multi-energy system.

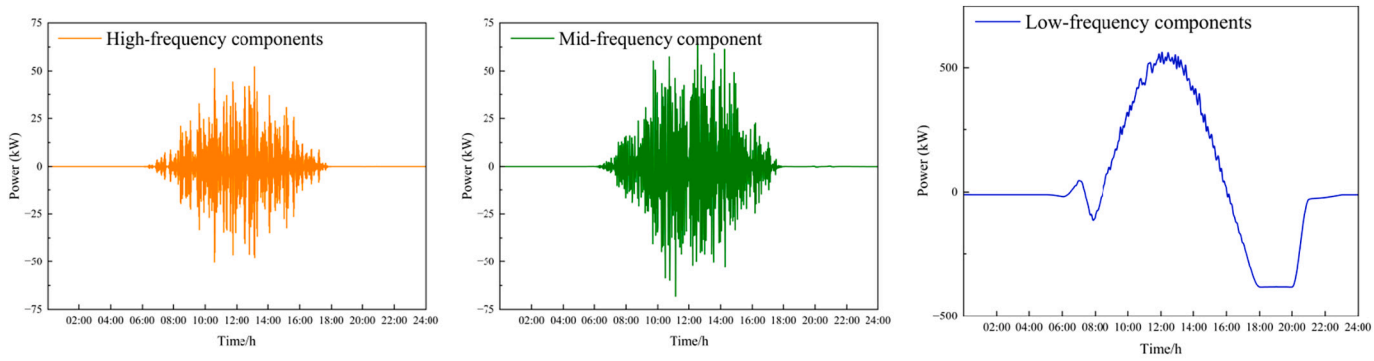


(a)Reconstituted high-frequency components

(b)Reconstructed mid-frequency component

(c)Reconstructed low-frequency component

**Fig. 23.** Refactoring components.

**Table 3**
System device parameters.

| Equipment | Parameter | Numeric Value |
|---|---|---|
| PV | $S_{PV}$/(USD/kWh) | 1.38 |
| SC | $S_{sc\_discharge}$/$S_{sc\_charge}$/(USD/kW) | 206.52 |
| | $I_{sc}$/(USD/kWh) | 564.5 |
| | $\eta_{sc}$ | 0.95 |
| | SOCmin sc ~ SOCmax sc | 0.1–0.8 |
| | $SOC_{sc0}$ | 0.5 |
| | *P*max sc(kW) | 200 |
| | $N_{sc}$ | 10 |
| HP [48] | $S_{HP}$/(USD/kWh) | 311.16 |
| | $\eta_{HP}$ | 0.98 |
| | *P*max HP(kW) | 200 |
| WST [49] | $I_{heat}$/(USD/kWh) | 9.64 |
| | $S_{WST}$/(USD/kWh) | 0.02 |
| | *SOC*min WST ~ *SOC*max WST | 0–1 |
| | $SOC_{WST}(0)$ | 0.5 |
| | $\eta_{WST}$ | 0.98 |
| | $IC_{WST}$(kWh) | 45,000 |
| EL [47] | $\eta_{EL}$ | 0.6 |
| | $\eta_{HEL}$ | 0.16 |
| | $I_{HESS}$/(USD/kWh) | 206.52 |
| | $S_{charge}$(USD/kW) | 0.04 |
| | $\eta_{FC}$ | 0.6 |
| FC | $\eta_{HFC}$ | 0.16 |
| | $I_{HESS}$/(USD/kWh) | 206.52 |
| | $S_{discharge}$/(USD/kW) | 0.12 |
| HST | $I_{HESS}$/(USD/kWh) | 12.39 |
| | $N_{HST}$/(USD/kg) | 61.95 |
| | *SOC*min HST ~ *SOC*max HST | 0–1 |
| | $SOC_{HST}(0)$ | 0.4 |
| | $\eta_{HST}$ | 0.98 |
| | *m*min HST/(kg) | 4000 |
| Grid tariffs [50] | *S*im grid(USD/kWh) | 0.11 |
| | *S*ex grid(USD/kWh) | 0.07 |

Fig. 26(c) illustrates the operation of the WST under Strategy 3. From 07:22 onward, the WST and the heat load of the users received heat generated by the HP. It significantly reduced the heat released by the WST. During 11:27 to 16:00 min period, as the SOC of the WST reached the threshold value of 0.7, some low-frequency components were redirected to the municipal grid instead of being supplied to the HP. This mechanism ensured efficient thermal energy management and prevented overcharging of the WST.

Fig. 26(d) illustrates the operation profile of the municipal grid in the Strategy 3. The grid supported the HP function in the thermal energy system from 7:22 to 8:53 and supplied low-frequency components of the differential power to the SC from 11:27 to 16:07. This dual role of the grid enhanced the flexibility and reliability of the multi-energy storage system.

### 6.4. Energy storage SOC and economic analysis

The SOC curves of energy storage devices in the three strategies are shown in the Fig. 27(a), (b), (c).

The construction and O&M costs of SC, HP systems, HESS, and PV were calculated and compared in the three strategies, as shown in Table 4.

As shown in Table 4, Strategy 2 achieves significant improvements in technical performance, successfully reducing the SOC limit exceedance time by 10.5 percentage points (from 47.5% to 37%) and completely eliminating system saturation. Although the adaptive power redistribution mechanism employed by Strategy 2 can effectively avoid SOC anomalies, the cost is that it forces the hybrid energy storage system—a high-cost component—to frequently operate in low-efficiency regions or non-optimal partial load conditions in order to offset the dynamic effects of power transfers.

In contrast, Strategy 3 fundamentally reconstructs this trade-off by connecting to the power grid. This strategy completely eliminates SOC limit exceedance time (reducing it to 0%). From a system perspective, the urban power grid can be regarded as a flexible buffer with almost unlimited capacity, capable of absorbing fluctuating power that would otherwise force the hybrid energy storage system or SCs into low-efficiency operation.

As shown in Table 5, although Strategy 2 completely eliminates system saturation, this performance improvement comes at the cost of economics, with a total cost 5.3% higher than Strategy 1. Although real-time power regulation can prevent SOC violations, it may force the HESS to operate more frequently under partial load or transient conditions, where its conversion efficiency is lower. Coupled with the higher unit cost of HESS, this increases the overall cost. Strategy 3, by connecting to the grid, significantly reduces the total cost by 13.3% and 17.7% compared with Strategies 1 and 2, respectively. The key to the cost reduction lies in the role of the municipal power grid as a flexible, large-scale 'virtual battery.' It achieves energy arbitrage by absorbing excess low-frequency electricity (preventing heat waste as seen in Strategy 1) and supplying power when needed, allowing dedicated storage devices to operate closer to their optimal points and avoid incurring high costs. This mechanism not only enhances the system's economic efficiency but also avoids high costs such as heat wastage caused by system constraints in Strategy 1.

The above results indicate that introducing external flexible resources into a multi-energy storage system is key to achieving the synergistic optimization of technical performance and economic benefits. Grid access can provide additional operational flexibility and effectively overcome the technical and economic bottlenecks in the dynamic regulation of the original system. The evolution from Strategy 1 to Strategy 3 reveals the inherent trade-offs in system operation: Strategy

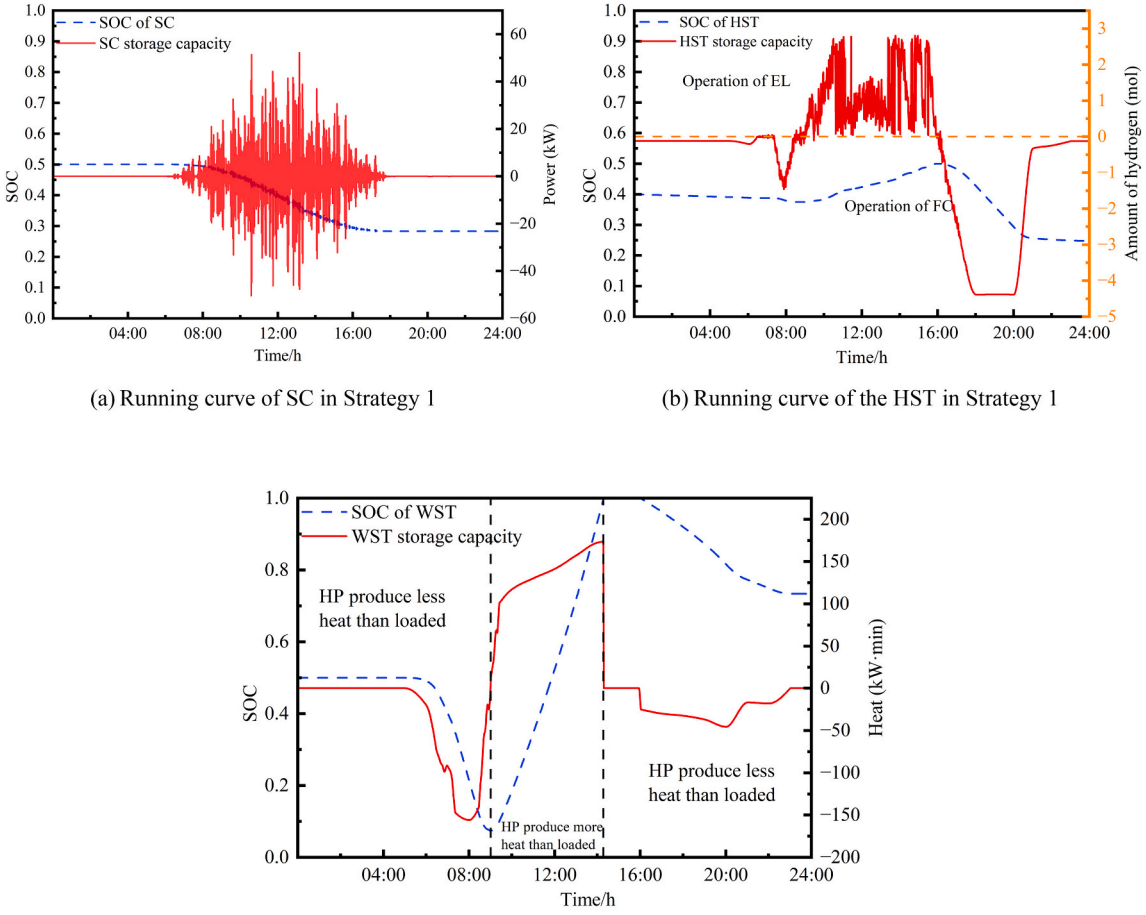


**Fig. 24.** Operating curves of each energy storage device under Strategy 1.

1, as the baseline, has significant state-of-charge management deficiencies (47.5% of time exceeding limits) and ECR = 28.73%; Strategy 2 greatly improves technical performance through real-time state-of-charge feedback (time exceeding limits reduced to 37%, ECR = 0%) but results in a 5.3% increase in operating costs, highlighting the technical-economic conflict; Strategy 3, through coordinated integration with the grid, ultimately resolves this conflict, achieving both perfect technical performance (0% exceeding limits, 0% ECR) and the lowest operating cost (13.3% and 17.7% lower than Strategies 1 and 2, respectively). This demonstrates that the combination of virtual inertia allocation, adaptive state-of-charge control, and grid coordination is a necessary approach to fully unlocking the synergistic potential of a multi-energy storage system integrating electricity, heat, and hydrogen.

The electro-thermal-hydrogen multi-energy storage system and its hierarchical control strategy proposed in this work are inherently scalable and modular. This design enables their potential extension to urban and regional energy networks. Operational findings further provide a practical basis for broadening the technology's applicability. Core components—including hydrogen storage, thermal storage, and supercapacitors—can be standardized and deployed modularly, while regional coordination is facilitated through a "centralized optimization, distributed control" architecture. Within such expanded systems, municipal power grids may act as flexible regulating resources, thereby improving resilience to renewable intermittency and amplifying the system's overall role in integrated energy management. The system design can also accommodate diverse electricity market structures, a feature that enhances its economic viability and operational practicality. Besides energy arbitrage, the system can proactively participate in ancillary service markets, including frequency regulation and reserve capacity provision.

## 7. Conclusions

This study establishes a clear research pathway from the validation of core algorithms to the performance evaluation of the entire system. The constructed experimental platform, centered on the supercapacitor-battery subsystem, conducts rigorous verification on the basic power allocation logic based on VMD and the real-time regulation principle based on SOC. The experimental results of this subsystem are highly consistent with the simulation results, confirming the reliability of the established basic models and control strategies. This validation outcome not only lays the necessary foundation for the subsequent application of the aforementioned strategies to the simulation of the integrated electrical-thermal-hydrogen system in the Beijing community case but also provides sufficient theoretical basis for this application. Based on the comprehensive analysis above, the following conclusions are drawn:

In this paper, an electrical-thermal-hydrogen multi-energy storage system incorporating SCs, WSTs and HSTs was constructed. The VMD method is proposed to divide the power frequency of the source-load difference power, thereby obtaining the output power of multiple energy storage devices. The effectiveness of the proposed strategy is validated through experimental studies.

The experimental platform was utilized to validate three distinct strategies: The baseline VMD frequency division strategy (Strategy 1), the VMD combined with timely re-frequency division strategy (Strategy 2) and the VMD allocation strategy with grid participation in regulation

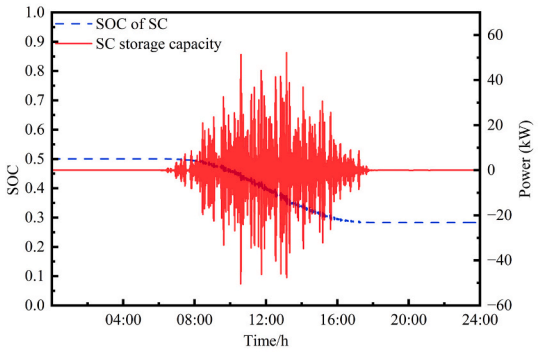


(a) Running curve of the SC in Strategy 2

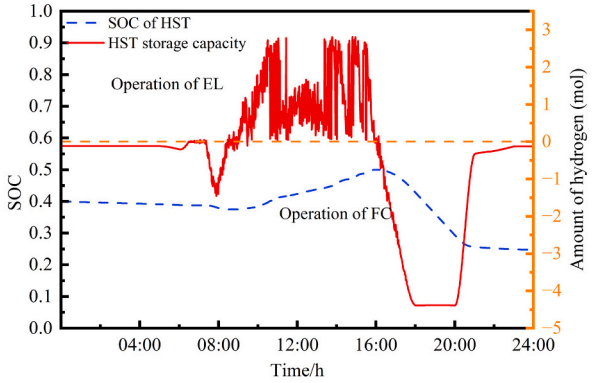


(b) Running curve of the HST in Strategy 2

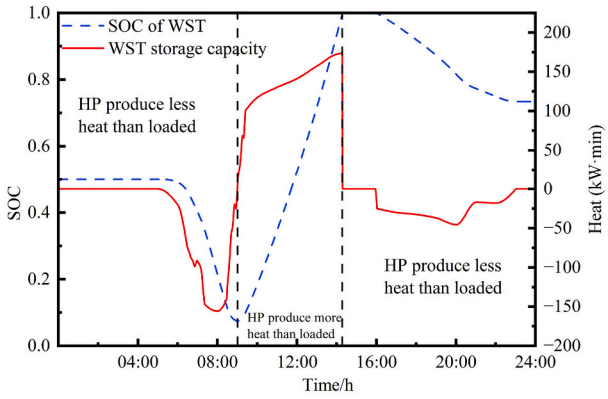


(c) Running curve of the WST in Strategy 2

**Fig. 25.** Operating curves of each energy storage device under Strategy 1.

(Strategy 3). The experimental results showed that the operational changes of the supercapacitor and lithium iron phosphate battery had an error margin of less than 0.2 kW compared to the simulation results. Once the SC began to respond, the municipal power grid ceased its response. By comparing the experimental results with the simulation results, the feasibility of the three strategies in improving power quality and enhancing the economic efficiency of equipment operation was confirmed.

Through the case analysis, it is observed that in Strategy 1, which was based on the VMD method, a significant SOC over-limit phenomenon occurred during the operation of the WST, with the out-of-limit time accounted for 47.5% of the total operation period. The timely redivision strategy 2 reduced the out-of-limit time for SCs and WSTs by 37%, but the operational cost of the equipment increases by 5.3% compared to Strategy 1. Building upon Strategy 2, Strategy 3, which involved municipal grid participation in regulation and control. It further reduced the out-of-limit time to 0%. Additionally, the operational cost of the equipment was reduced by 13.3% and 17.7% compared to Strategy 1 and Strategy 2. In this study, the municipal power grid is not just a backup power source, but a transformative driver that can promote the coordination and economic operation of heterogeneous energy storage technologies.

However, the practical implementation of the proposed strategies must consider several unmodeled dynamics and external factors. Although this study has verified the technical feasibility of the proposed system and corresponding strategies, to provide clear directions for future research, it is still necessary to clarify its inherent limitations. This study focuses on the short-term operational optimization of the system during typical working days and has not yet analyzed the system's stability under long-term cyclical operational scenarios, nor has it quantified the impact of aging of core equipment on the system's overall performance and economic benefits. Besides, the stability of transient processes is also a key issue in actual operation. Therefore, future work will establish a dynamic model of the integrated electricity-heat-hydrogen system. This model will facilitate a transient stability analysis and incorporate equipment lifetime degradation modeling. Building upon this foundation, a comprehensive life-cycle assessment framework will be developed. By integrating these equipment aging models, the assessment aims to critically evaluate and enhance the system's long-term engineering feasibility.

In addition, the practical engineering implementation of this system still faces real-world challenges such as scaling bottlenecks and high initial capital investment. Prior to actual deployment, targeted techno-economic analyses and evaluations of return on investment need to be conducted, taking into account the characteristics of regional energy markets and policy environments. Future research will further aim to develop robust optimization models to effectively address uncertainties in renewable energy output forecasts and load demand predictions; at the same time, it will explore the system's adaptation pathways for participating in complex electricity market transactions, thereby enhancing its overall economic benefits and market competitiveness.

## CRediT authorship contribution statement

**Di Wu:** Writing – review & editing, Project administration. **Shiyang Yu:** Writing – review & editing, Writing – original draft, Software. **Ao Liu:** Software. **Zhijian Liu:** Software, Methodology. **Zhuoying Liang:** Software. **Shicong Zhang:** Funding acquisition. **Xinyan Yang:** Writing – review & editing. **Guiqiang Li:** Methodology. **Wentao Wu:** Funding acquisition.

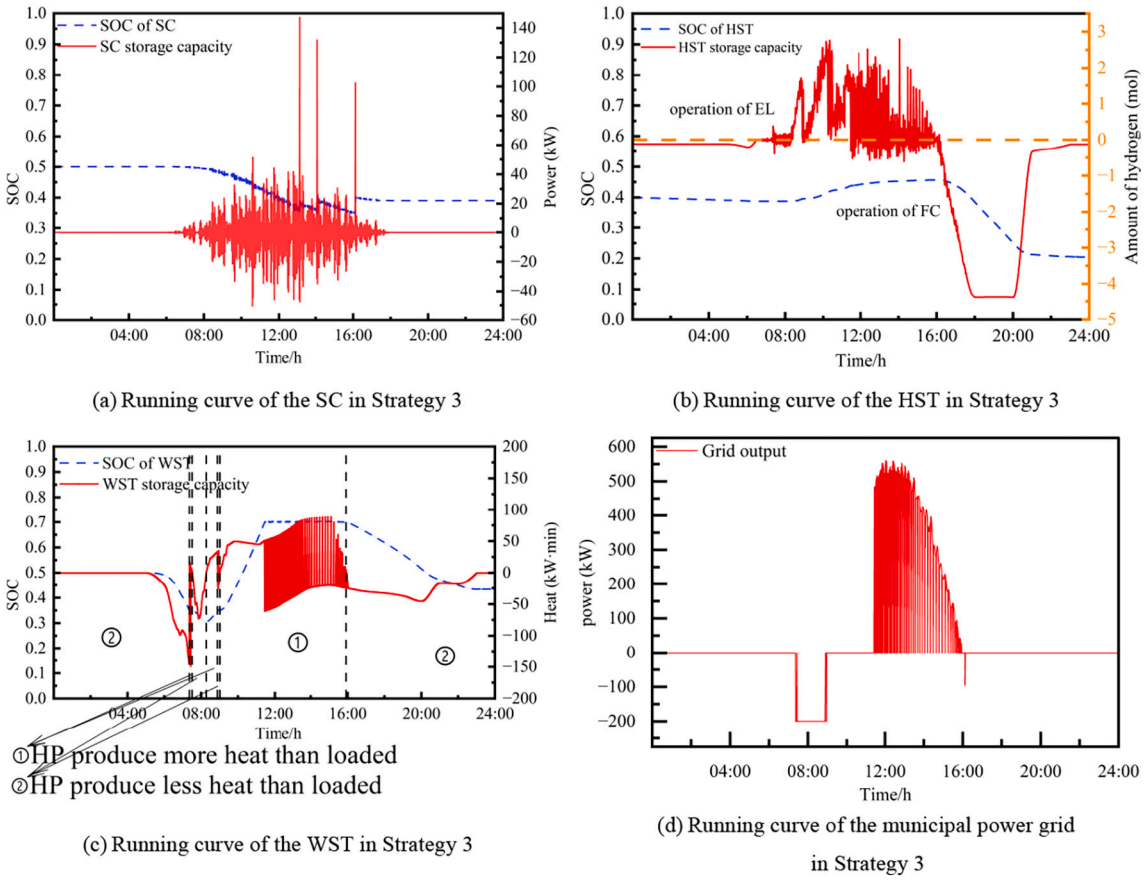


**Fig. 26.** Operating curves of various energy storage devices and the municipal power grid under Strategy 3.

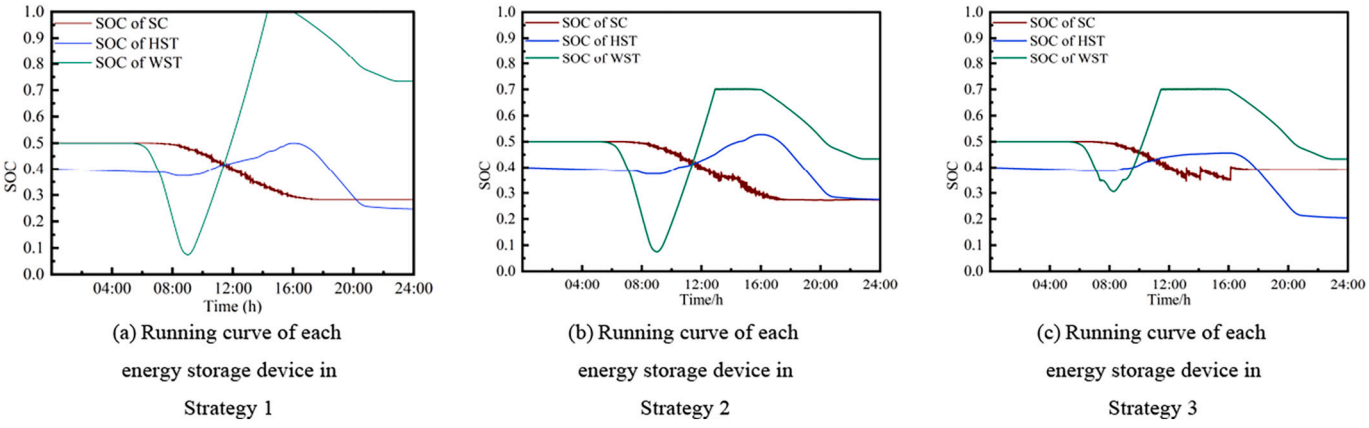


**Fig. 27.** Operating curves of each energy storage device under the three strategies.

**Table 4**
The proportion of out-of-limit time and the ECR of the energy storage system of the three strategies.

| Evaluation indicators | Percentage of out-of-limit time (%) | *ECR*(%) |
|---|---|---|
| Strategy 1 | 47.5 | 28.73 |
| Strategy 2 | 37 | 0 |
| Strategy 3 | 0 | 0 |

## Funding

The relevant funding projects and numbers for this article are as follows:

1. National Natural Science Foundation of China (No. 52206247)
2. Natural Science Foundation of Hebei Province (No. E2023502040)
3. Hebei Province Higher Education Institutions Scientific Research Project (No. BJ2025033)
4. National Key R&D Program of China (No. 2022YFE0117200).

## Declaration of competing interest

The authors declare that we have no known competing financial interests or personal relationships that could have appeared to influence

**Table 5**
Cost comparison of the three scenarios.

| COST | $C_{HPSS}$(USD) | $C_{HESS}$(USD) | $C_{PV}$(USD) | $C_{SC}$(USD) | $C_{grid}$(USD) | $C_{total}$(USD) |
|---|---|---|---|---|---|---|
| Strategy 1 | 23,519 | 578,717 | 506 | 10,827 | 0 | 613,569 |
| Strategy 2 | 19,210 | 615,581 | 506 | 10,834 | 0 | 646,131 |
| Strategy 3 | 19,124 | 501,265 | 506 | 10,886 | 25 | 531,756 |

the work reported in this paper.

## Appendix A. Supplementary data

Supplementary data to this article can be found online at https://doi.org/10.1016/j.est.2026.120542.

## Data availability

No data was used for the research described in the article.

## References


[1] J. Lou, S. Yu, R.Y. Cui, A. Miller, N. Hultman, A provincial analysis on wind and solar investment needs towards China's carbon neutrality, Appl. Energy 378 (2025) 124841, https://doi.org/10.1016/j.apenergy.2025.124841.

[2] C. Wang, H. Chen, Z. Wang, Y. Gao, G. Zhang, Economic assessment and grid parity analysis of photovoltaic power generation considering tradable green certificate, Appl. Energy 382 (2025) 125282, https://doi.org/10.1016/j.apenergy.2025.125282.

[3] A.-K. von Krauland, M.Z. Jacobson, India onshore wind energy atlas accounting for altitude and land use restrictions and co-located solar, Cell Rep. Sustain. 1 (2024) 100083, https://doi.org/10.1016/j.crsus.2024.100083.

[4] S. Miyake, S. Teske, J. Rispler, M. Feenstra, Solar and wind energy potential under land-resource constrained conditions in the Group of Twenty (G20), Renew. Sust. Energ. Rev. 202 (2024) 114622, https://doi.org/10.1016/j.rser.2024.114622.

[5] L.G. Tapia Carpio, F.A.C. Guimarães, Regional diversification of hydro, wind, and solar generation potential: a mean-variance model to stabilize power fluctuations in the Brazilian integrated electrical energy transmission and distribution system, Renew. Energy 235 (2024) 121266, https://doi.org/10.1016/j.renene.2024.121266.

[6] B. Wang, B. Zhaoxiang, Hydrogen energy storage: mitigating variability in wind and solar power for grid stability in Australia, Int. J. Hydrog. Energy 97 (2025) 1249–1260, https://doi.org/10.1016/j.ijhydene.2025.02.001.

[7] M.R. Elkadeem, A. Younes, J. Jurasz, A.S. AlZahrani, M.A. Abido, A spatio-temporal decision-making model for solar, wind, and hybrid systems – a case study of Saudi Arabia, Appl. Energy 383 (2025) 125277, https://doi.org/10.1016/j.apenergy.2025.125277.

[8] J. Liu, J. Hu, Q. Wan, J. Ming, C. Shuai, Energy services for solar PV projects: exploring the accessibility and affordability of clean energy for rural China, Energy 299 (2024) 131442, https://doi.org/10.1016/j.energy.2024.131442.

[9] I.H. Ahmed, K.A. Alakoul, A. Al-Manea, A.R.H. Wetaify, K. Saleh, R. Al-Rbaihat, A. Alahmer, An overview of hydrogen production techniques: challenges and limiting factors in achieving wide-scale productivity, AIP Conf. Proc. 3051 (1) (2024) 050003, https://doi.org/10.1063/5.0191762.

[10] F. Li, C. Wang, Z. Liu, Y. Huang, T. Wang, Sparrow search algorithm-optimized variational mode decomposition-based multiscale convolutional network for cavitation diagnosis of hydro turbines, Ocean Eng. 312 (2024) 119055, https://doi.org/10.1016/j.oceaneng.2024.119055.

[11] L. Xing, Y. Liu, An optimization capacity design method of wind/photovoltaic/hydrogen storage power system based on PSO-NSGA-II, Energy Eng. 120 (2023) 1023–1043, https://doi.org/10.32604/ee.2023.030541.

[12] Y. Houam, N. Bouarroudj, A. Djari, A. Si Tayeb, Reliable and cost-effective optimal design of an off-grid hybrid renewable energy system using a multi-objective swarm intelligence method considering long-term effects of high temperature, Energy Convers. Manag. 315 (2024) 118754, https://doi.org/10.1016/j.enconman.2024.118754.

[13] J. Shi, W. Huang, N. Tai, F. Fan, M. Yu, Z. Ma, Power fluctuation mitigation strategy for distributed renewable energy in combined electricity-heat microgrid, Proc. CSEE 38 (02) (2018), https://doi.org/10.13334/j.0258-8013.pcsee.170011.

[14] M. Chen, J. Wei, X. Yang, Q. Fu, Q. Wang, S. Qiao, Multi-objective optimization of multi-energy complementary systems integrated biomass-solar-wind energy utilization in rural areas, Energy Convers. Manag. 323 (2025) 119241, https://doi.org/10.1016/j.enconman.2025.119241.

[15] J. Zhou, D. Liu, C. Yang, Y. Wang, S. Yang, Y. Wu, Coupling geospatial suitability simulation and life cycle carbon emissions towards uncertain optimization planning for wind-photovoltaic-hydrogen multi-energy complementary system, Energy Convers. Manag. 321 (2024) 119103, https://doi.org/10.1016/j.enconman.2024.119103.

[16] C.K.R. Pocha, W.Y. Chia, Silvanir, T.A. Kurniawan, K.S. Khoo, K.W. Chew, Thermochemical conversion of different biomass feedstocks into hydrogen for power plant electricity generation, Fuel 340 (2023) 127472, https://doi.org/10.1016/j.fuel.2023.127472.

[17] L. Hou, X. Tong, H. Chen, L. Fan, T. Liu, W. Liu, T. Liu, Optimized scheduling of smart community energy systems considering demand response and shared energy storage, Energy 295 (2024) 131066, https://doi.org/10.1016/j.energy.2024.131066.

[18] L. Zhang, Q. Li, Y. Fang, Y. Yang, H. Ren, L. Fan, N. Tai, Optimization scheduling of community integrated energy system considering integrated demand response, J. Build. Eng. 98 (2024) 111230, https://doi.org/10.1016/j.jobe.2024.111230.

[19] Z. Wang, B. Du, Y. Li, C. Xie, H. Wang, Y. Huang, P. Meng, Multi-time scale scheduling optimization of integrated energy systems considering seasonal hydrogen utilization and multiple demand responses, Int. J. Hydrog. Energy 67 (2024) 728–749, https://doi.org/10.1016/j.ijhydene.2024.04.015.

[20] Q. Lu, W. Zeng, Q. Guo, S. Lü, Optimal operation scheduling of household energy hub: a multi-objective optimization model considering integrated demand response, Energy Rep. 8 (2022) 15173–15188, https://doi.org/10.1016/j.egyr.2022.11.014.

[21] X. Wu, L. Yang, B. Zheng, Joint capacity configuration and demand response optimization of integrated energy system considering economic and dynamic control performance, Energy 301 (2024) 131723, https://doi.org/10.1016/j.energy.2024.131723.

[22] S. Li, F. Cai, S.J. Abbas, A.K. Dutta, S. Shomurotova, Y. Elmasry, A multi-objective analysis for enhanced energy and exergy performances of an integrated compressed air energy storage system using the meta-heuristic whale optimization algorithm, J. Energy Storage 105 (2025) 114681, https://doi.org/10.1016/j.est.2025.114681.

[23] Z. Mohammadi, S. Rahimi, M. Fallah, H. Siyahi, M. Siyahi, Proposal and multicriteria optimization of an integrated energy system powered by solar energy and electrolysis to produce hydrogen, utilizing an organic flash combined power/cooling cycle with dual ejectors, Energy 315 (2025) 134329, https://doi.org/10.1016/j.energy.2025.134329.

[24] N. Sezer, S. Bayhan, Integrated solar-powered freeze desalination and water electrolysis system with energy recovery and storage for sustainable agriculture in desert environments, Desalination 595 (2025) 118321, https://doi.org/10.1016/j.desal.2025.118321.

[25] N.W. Hesty, K. Fauziah, T. Aminuddin, S.R. Zaky, M. Fithri, A. Aman, D. Aziz, R. P. Rostyono, Ifanda Wijayanto, A comprehensive analysis of wind power integrated with solar and hydrogen storage systems: case study of Java's Southern coast, Int. J. Hydrog. Energy (2024), https://doi.org/10.1016/j.ijhydene.2024.03.001.

[26] A.M. Ghaithan, Multi-objective model for designing hydrogen refueling station powered using on-grid photovoltaic-wind system, Energy 312 (2024) 133464, https://doi.org/10.1016/j.energy.2024.133464.

[27] O. Akdağ, Modeling and economic evaluation of hybrid renewable energy sources for green hydrogen production: a case study for the Mediterranean region, Renew. Energy 240 (2025) 122228, https://doi.org/10.1016/j.renene.2025.122228.

[28] S.A. Amirkhalili, A. Zahedi, A. Ghaffarinezhad, B. Kanani, Design and evaluation of a hybrid wind/hydrogen/fuel cell energy system for sustainable off-grid power supply, Int. J. Hydrog. Energy 100 (2025) 1456–1482, https://doi.org/10.1016/j.ijhydene.2025.01.001.

[29] P.C. Okonkwo, M.S. Islam, U.H. Taura, E.M. Barhoumi, I.B. Mansir, B.K. Das, M.M. B.A. Sulaiman, E.B. Agyekum, I. Bahadur, A techno-economic analysis of renewable hybrid energy systems for hydrogen production at refueling stations, Int. J. Hydrog. Energy 78 (2024) 68–82, https://doi.org/10.1016/j.ijhydene.2024.03.015.

[30] J. Xu, L. Liu, F. Wang, Equilibrium strategy-based economic-reliable approach for day-ahead scheduling towards solar-wind-gas hybrid power generation system: a case study from China, Energy 240 (2022) 122728, https://doi.org/10.1016/j.energy.2021.122728.

[31] X. Li, T. Li, L. Liu, Z. Wang, X. Li, J. Huang, J. Huang, P. Guo, W. Xiong, Operation optimization for integrated energy system based on hybrid CSP-CHP considering power-to-gas technology and carbon capture system, J. Clean. Prod. 391 (2023) 136119, https://doi.org/10.1016/j.jclepro.2023.136119.

[32] X. Leng, X. Sun, J. Xu, W. Huang, Optimal planning of a hybrid system integrating of combined cooling, heat and power and energy storage resources, Sustain. Energy Technol. Assess. 50 (2022) 101806, https://doi.org/10.1016/j.seta.2021.101806.

[33] J. Li, H. Chen, J. Li, Y. Zhang, P. Pan, J. Bian, Z. Yu, Bi-level optimization model of hydrogen-blended gas units and multi-type energy storage system considering low-carbon operation, Energy 314 (2025) 134162, https://doi.org/10.1016/j.energy.2025.134162.

[34] R. Wang, E. Akbari, L. Bagherzadeh, S. Pirouzi, Stochastic economic sizing of hydrogen storage-based renewable off-grid system with smart charge of electric vehicles according to combined hydrogen and power model, J. Energy Storage 108 (2025) 115171, https://doi.org/10.1016/j.est.2025.115171.

[35] T. Yi, Q. Li, Y. Zhu, Z. Shan, H. Ye, C. Xu, H. Dong, A hierarchical co-optimal planning framework for microgrid considering hydrogen energy storage and

demand-side flexibilities, J. Energy Storage 84 (2024) 110940, https://doi.org/10.1016/j.est.2024.110940.
[36] R. Al-Rbaihat, Sensitivity analysis of a hybrid PV-WT hydrogen production system via an electrolyzer and fuel cell using TRNSYS in coastal regions: a case study in Perth, Australia, Energies 18 (2025) 3108, https://doi.org/10.3390/en18123108.
[37] G. Xiao, F. Xu, L. Tong, H. Xu, P. Zhu, A hybrid energy storage system based on self-adaptive variational mode decomposition to smooth photovoltaic power fluctuation, J. Energy Storage 55 (2022) 105509, https://doi.org/10.1016/j.est.2022.105509.
[38] R. Hou, J. Liu, W. Chen, J. Liu, Enhancing stability of wind power generation in microgrids via integrated adaptive filtering and power allocation strategies within hybrid energy storage systems, J. Energy Storage 111 (2025) 115392, https://doi.org/10.1016/j.est.2025.115392.
[39] M. Gao, Z. Han, B. Zhao, P. Li, D. Wu, P. Li, Optimal planning method of multi-energy storage systems based on the power response analysis in the integrated energy system, J. Energy Storage 73 (2023) 109015, https://doi.org/10.1016/j.est.2023.109015.
[40] A.N. Akpolat, E. Dursun, A.E. Kuzucuoğlu, Modeling and operation of a fuel cell stack for distributed energy resources: a living lab platform, Int. J. Hydrog. Energy 75 (2024) 578–591, https://doi.org/10.1016/j.ijhydene.2024.01.001.
[41] Y. Zhang, S. Zhu, J. Lin, Experimental platform for electrically thermal integrated energy system based on flexible resource collaboration of source-load-storage, Lab. Res. Explor. 43 (07) (2024) 69–75.
[42] P.P. Golaki, M. Zarnoush, S.M. Zolfaghari, M. Soltani, M.A. Rosen, Comprehensive examination of a green hybrid biomass-integrated compressed air energy storage system with PEM hydrogen production across various operating modes, J. Energy Storage 121 (2025) 116545, https://doi.org/10.1016/j.est.2025.116545.
[43] C. Li, W. Qin, J. Wang, et al., A two-stage robust optimization for multi-timescale coordinated control of electro-hydrogen energy storage and demand response, J. Energy Storage 141 (Part A) (2026) 119077, https://doi.org/10.1016/j.est.2026.119077.
[44] H. Liu, X. Zhao, G. Li, et al., Investigation of a novel separately-configured micro-thermoelectric cooler to enabling extend application scope, Appl. Energy 306 (2022) 117941, https://doi.org/10.1016/j.apenergy.2021.117941.
[45] A. Liu, D. Wu, D. Gong, S. Yu, Z. Han, G. Li, Research on electricity-heat collaborative storage strategy of photovoltaic storage microgrid based on multiple energy storage, HVAC 54 (11) (2024) 131–139.
[46] G. Fan, Z. Liu, X. Liu, Y. Shi, D. Wu, J. Guo, S. Zhang, X. Yang, Y. Zhang, Two-layer collaborative optimization for a renewable energy system combining electricity storage, hydrogen storage, and heat storage, Energy 259 (2022) 125047, https://doi.org/10.1016/j.energy.2022.125047.
[47] U.S. Department of Energy (DOE), Hydrogen and fuel cell technologies office multi-year research, development, and demonstration plan, Retrieved from, https://www.energy.gov/eere/fuelcells/hydrogen-and-fuel-cell-technologies-office-multi-year-research-development-and, 2020.
[48] China Academy of Building Research, White Paper on the Techno-Economics of Building-Coupled Renewable Energy Systems. Beijing, 2022.
[49] IEA, Technology Roadmap - Energy Storage, IEA, Paris, 2014. Retrieved from, https://www.iea.org/reports/technology-roadmap-energy-storage. License: CC BY 4.0.
[50] Beijing Municipal Commission of Development and Reform, Notice on the 2023 Electricity Price Adjustment Targets and Time-of-Use Electricity Pricing Policy in the City, 2023.